DEPENDANCE OF RADIATIVE FORCING ON MINERALOGY IN THE COMMUNITY ATMOSHPERE MODEL

A Thesis

Presented to the Faculty of the Graduate School

of Cornell University

In Partial Fulfillment of the Requirements for the Degree of

Master of Science

by

Rachel Anne Scanza

January 2014

ABSTRACT

The mineralogy of desert dust is important due to its effect on radiation, clouds and biogeochemical cycling of trace nutrients. This study presents the simulation of dust as a function of both mineral composition and size at the global scale using mineral soil maps. Externally mixed bulk mineral aerosols in the Community Atmosphere Model version 4 (CAM4) and internally mixed modal mineral aerosols in the Community Atmosphere Model version 5.1 (CAM5) embedded in the Community Earth System Model version 1.0.3 (CESM) coordinated by the National Center for Atmospheric Research (NCAR) are speciated into common mineral components in place of total dust. The simulations with mineralogy are compared to available observations of mineral atmospheric distribution and deposition along with observations of clear-sky radiative forcing efficiency. Based on these simulations, we estimate the all-sky direct radiative forcing at the top of the atmosphere as +0.04 and +0.10 Wm^{-2} for CAM4 and CAM5 simulations with mineralogy and compare this with simulations of dust with optimized optical properties, wet scavenging and particle size distribution in CAM4 and CAM5 of -0.05 and -0.11 Wm^{-2}, respectively. The ability to correctly include the mineralogy of dust in climate models is hindered by its spatial and temporal variability as well as insufficient global in-situ observations, incomplete and uncertain source mineralogies and the uncertainties associated with data retrieved from remote sensing methods.

BIOGRAPHICAL SKETCH

Rachel Anne Scanza was born in Los Angeles, California and graduated from Westlake High School. During her undergraduate studies at University of California, San Diego, her myriad academic interests ranged from creative writing to mechanical engineering. In the process of completing the required coursework for entry into medical school, she found that her interests and abilities were in mathematics and chemistry, prompting a switch from Literature/Creative Writing and Pre-med to Chemistry. During her final semester, as an elective she took Atmospheric Chemistry which catalyzed her interest in Atmospheric Science (as opposed to the pharmaceutical applications inherent with Organic Chemistry). Nevertheless, after completing a Bachelors of Science in Chemistry from the University of California, San Diego, she joined the workforce as an assistant to the manager of a company involved in pharmaceutical drug trials. While working, she began looking into graduate programs that focused on Atmospheric and Planetary Science. She applied to Cornell University's Earth and Atmospheric Science department and was fortunately accepted as a graduate student with Dr. Natalie Mahowald. Rachel learned to work with and modify the Community Earth System Model, a global climate model, to include mineralogy in place of dust. The work involved in modifying two atmosphere models embedded in CESM and the results obtained from model simulations is the subject of this thesis.

For Mom, Dad, Fred, Sherry and Spike.

ACKNOWLEDGMENTS

I would like to acknowledge the guidance, wisdom and patience of my adviser Dr. Natalie Mahowald. With her encouragement and support, I was able to achieve this point in my academic career. Additionally, I would like to acknowledge my committee members Dr. Peter Hess and Dr. Lou Derry, whose classes taught me valuable knowledge in Atmospheric Science and whose discussions with and comments from greatly improved the quality of this document.

I would also like to acknowledge my colleagues, in particular Nick Heavens, Daniel Ward, Qi Tang, and Samuel Albani for their help and most of all patience with computer modeling and general help with problems or questions that arose during the last several years. Also I would like to acknowledge Jasper Kok, Yan Zhang, Steve Ghan, Xiaohong Liu and Charlie Zender whose help and collaborations made this document possible. In addition, I would like to thank the graduate students who have been sources of help and friendship, Andrew Melkonian, Jennifer Jay, Felipe Aron, Scott Henderson, Anastasija Cabalova, Wenxiu Sun, Diego Quieros, Yun Zheng, Aaron Perry and everyone in Bradfield Hall and Snee Hall who wasn't previously mentioned.

Most of all, I wish to thank my family, whose unconditional love and support have been my sustenance.

TABLE OF CONTENTS

Biographical Sketch……..……iii

Dedication…….…….……...……iv

Acknowledgements……..…….……v

Table of Contents…….....……..vi

List of Figures……..……..……..……vii

List of Tables…….……ix

1.0 Introduction…….……...…..1

2.0 Methods…….…….…….…….……4
2.1 Desert Dust Model…….……...…….4
2.2 Conversion of Soil Mineralogy to Aerosol Mineralogy..……..…..….9
2.3 Modeling of Radiation……..…..…..…11
2.4 Description of Simulations…….…….…….……..13
2.5 Comparison to Observations……..…...…….…….15

3.0 Results……...…….…..……19
3.1 Desert Dust Mineralogical Distribution…….…..…19
3.2 Aerosol Optical Depth and Single Scattering Albedo…….....……27
3.3 Radiative Forcing……..…..…31
3.3.1 Clear-sky Radiative Forcing…….....……31
3.3.2 All-sky Radiative Forcing…….....……35
3.4 Sensitivity to Size…….....……39
3.5 Quantifying Uncertainty…….…….……41

4.0 Discussion and Conclusion…….…….…....……43

Bibliography……....…..45

LIST OF FIGURES

Figure 1: Mineral fraction maps for CAM4 and CAM5 based on work by Claquin et al. (1999). Illite (a), Kaolinite (b), Montmorillonite (c) are clay-sized (0-2μm). Hematite (d) has the same distribution for both clay-sized and silt-sized (2-20μm). Quartz (e), Calcite (f), Feldspar (g), Gypsum (h) and Other-coarse (i) silt-sized. CAM4 includes Illite (a), Kaolinite (b), Montmorillonite (c), Hematite (d), Quartz (e), Calcite (f), Feldspar (g), and Gypsum (h). CAM5 includes Illite (a), Kaolinite (b), Montmorillonite (c), Hematite (d) and Other-Coarse (i) which represents quartz, calcite, feldspar, and gypsum. **(Page 19)**

Figure 2: Total percent column mineral distributions for CAM4 shown as the sum of all four bins for each mineral. Hematite (f) and Gypsum (h) are scaled by 10 so that they can be visually compared with Illite (a), Kaolinite (b), Montmorillonite (c), Quartz (d), Calcite (e) and Feldspar (g). **(Page 20)**

Figure 3: Total percent column mineral distributions for CAM5 shown as the sum of the fine mode (mode 1) and coarse mode (mode 3) for each mineral. Hematite (d) is scaled by 10 so that it can be visually compared with Illite (a), Kaolinite (b) and Montmorillonite (c). **(Page 21)**

Figure 4: Relative mass abundance of minerals as modeled compared to observations from Kandler et al. (2009) for CAM4, bins 1-4, and CAM5, mode 1 and mode 3. The CAM4 comparison is for Quartz (c), Calcite (d), Feldspar (f) and Gypsum (g). Comparisons for CAM4 and CAM5 include Illite (a), Kaolinite (b) and Hematite (e). **(Page 22)**

Figure 5: Kaolinite/Illite mineral ratio of bulk dry deposition from CAM4 and CAM5 (kg K/ kg I) compared to bulk observational ratios (kg K/ kg I) from field work by Shen et al. (2005), Glaccum and Prospero (1980), Kandler et al. (2009), Prospero and Bonatti (1969), Caquineau et al. (1998), Kiefert et al. (1996) and Falkovich et al. (2001). **(Page 23)**

Figure 6: Hematite/Illite mineral ratio of bulk dry deposition from CAM4 and CAM5 (kg H/ kg I) compared to bulk observational ratios (kg H/ kg I) from field work by Engelbrecht et al. (2009b) and Kandler et al. (2009). **(Page 24)**

Figure 7: Kaolinite/Illite mineral ratio of wet and dry deposition for bin 1 and bin 2 from CAM4 (a) (kg K/kg I) and from characteristic basal X-ray diffraction maxima ratios of K/I of ocean core sediments (b) (Biscaye 1965). Data is segregated by latitude bands in scatterplot (c). **(Page 25)**

Figure 8: Kaolinite/Illite mineral ratio of wet and dry deposition for mode 1 from CAM5 (a) (kg K/kg I) and from characteristic basal X-ray diffraction maxima ratios

of K/I of ocean core sediments (b) (Biscaye 1965). Data is segregated by latitude bands in scatterplot (c). **(Page 26)**

Figure 9: Modeled Aerosol Optical Depth (a,b), Absorbing Aerosol Optical Depth (c,d) and Single Scattering albedo (e,f) compared to AERONET retrievals at sites where modeled $AOD_{dust} > AOD_{total}*0.5$. CAM4 (a,c,e) and CAM5 (b,d,f) are shown. **(Page 29)**

Figure 10: Model Single Scattering Albedo in CAM4 mineralogy is compared to total percent column hematite (a) and total percent column black carbon (b). The location of AERONET sites used in the comparison in Figure 9 are plotted in blue. **(Page 30)**

Figure 11: Model Single Scattering Albedo from CAM5 with mineralogy is compared to total percent column hematite (a) and total percent column black carbon (b). The location of AERONET sites used in the comparison in Figure 9 are plotted in blue. **(Page 30)**

Figure 12: Model Single Scattering Albedo for CAM4 with tuned dust (a), CAM5 with tuned dust (b), CAM4 with mineralogy (c), and CAM5 with mineralogy (d). **(Page 34)**

Figure 13: Spatial distribution of annual all-sky radiative forcing (SW+LW) at the top of atmosphere for CAM4 with tuned dust and with mineralogy (a,c) and for CAM5 with tuned dust and mineralogy (b,d). **(Page 37)**

Figure 14: Spatial distribution of annual all-sky radiative forcing (SW+LW) at the surface for CAM4 with tuned dust and with mineralogy (a,c) and for CAM5 with tuned dust and mineralogy (b,d). **(Page 38)**

Figure 15: Modeled Aerosol Optical Depth (a,b), Absorbing Aerosol Optical Depth (c,d) and Single Scattering albedo (e,f) compared to AERONET retrievals at sites where modeled $AOD_{dust} > AOD_{total}*0.5$. CAM4 (a,c,e) and CAM5 (b,d,f) are shown for tuned dust, mineralogy, and tuned dust + release size. **(Page 40)**

LIST OF TABLES

Table 1: Mean Mineralogical Table from Claquin et al. 1999. Gypsic xerosols and yermosols (Xy,Yy), Gleyic Solontchaks, (Zg), Orthic Solontchaks (Zo) and salt flats (ST) are renormalized to 100. Hematite is added to the clay fraction by subtracting the mass from Illite following Balkanski et al., 2007. **(Page 7)**

Table 2a: The fraction of dust aerosol mass contributed by the soil clay and silt fractions for each of the 4 particle size bins for the bulk scheme in CAM4 from work by Kok 2011. **(Page 8)**

Table 2b: The fraction of dust aerosol mass contributed by the soil clay and silt fractions for each of the 2 particle modes for the modal scheme in CAM5 from work by Kok 2011. **(Page 8)**

Table 3: Refractive indices of minerals used , wavelengths of refractive indices and references for input into CAM4 and CAM5. Refractive indices specified as Zender are a Maxwell-Garnet internal mixture of 48% quartz, 25% illite, 25% montmorillonite and 2% calcite by volume. These were used primarily to simplify the comparison of CAM4 and CAM5. Longwave optics for CAM4 were taken from CAM3 because a solver was not available to calculate the absorption coefficients. **(Page 12)**

Table 4: Description of the model simulations used in this study. All cases are for three years with the third year used for comparisons to observations and for RF calculations. All cases are run at 1.9°x2.5° resolution. FSDBAM indicates bulk aerosols, active atmosphere, land and sea ice components, data ocean, slab glacier and GEOS5 meteorology. FC5 indicates modal aerosols, stand-alone atmosphere with land and sea ice components, data ocean, slab glacier, model winds and CAM5 physics. **(Page 14)**

Table 5: Observations of mineralogy used to evaluate simulated mineral distributions in CAM4 and CAM5. Data that is suspended near the surface was chosen in order to compare to dry deposition in the models. Ocean core sediment data is compared to bulk dry and wet deposition. **(Page 15)**

Table 6a: The mean and standard deviation for AERONET (Holben et al., 1998, 2001) retrivals and the mean for CAM4 with tuned dust (CAM4-t) and mineralogy (CAM4-m) and CAM5 with tuned dust (CAM5-t) and mineralogy (CAM5-m) for Aerosol Optical Depth, Absorbing Aerosol Optical Depth and Single Scattering Albedo at AERONET sites where $AOD_{dust} > 0.5*AOD_{total}$. **(Page 29)**

Table 6b: The standard deviation in the model over the standard deviation in AERONET. Values less than 1 indicate that the model is not capturing the dynamic range from the observations while values greater than 1 indicate the model is simulating a larger range than observed. This metric is used to test whether the simulations with mineralogy are better capturing the range in the observations, with blue denoting a decrease in ability and red signifying an increase. **(Page 29)**

Table 7: Comparison of observed top of atmosphere clear-sky radiative forcing efficiencies ($Wm^{-2}\tau^{-1}$) over N. Atlantic and N. Africa regions with simulated RFE. Simulations are for CAM4 and CAM5 with release dust, tuned dust, tuned dust and release size distribution, and mineralogy. **(Page 32)**

Table 8a: Simulated annual average all-sky radiative forcing. **(Page 36)**

Table 8b: Simulated regional annual average all-sky radiative forcing. For comparison, regions are from Yoshioka et al. 2007. **(Page 36)**

Table 9: Percent change in annual all-sky radiative forcing for CAM4 and CAM5 from tuned to tuned + release size, tuned to mineralogy and tuned + release size to mineralogy. **(Page 41)**

CHAPTER 1

1.0 INTRODUCTION

Dust aerosols are soil particles suspended in the atmosphere, and they impact the climate system by influencing the radiation budget, cloud processes (Miller and Tegen, 1998;Mahowald and Kiehl, 2003;Karydis et al., 2011;DeMott et al., 2003;Levin et al., 2005), and various biogeochemical cycles (Swap et al., 1992;Martin et al., 1991;Jickells et al., 2005). The radiation balance of the Earth system is affected by the scatter and absorption of solar and infrared radiation by mineral aerosols (Miller and Tegen, 1998;Sokolik and Toon, 1999). Both magnitude and sign of radiative forcing of dust is considered to by one the most uncertain aspects in determining the net radiative forcing from aerosols (IPCC, 2007). Previous and ongoing modeling efforts address the importance of determining the mineral composition of dust and its impact on the dust radiation budget (Sokolik and Toon, 1999;Claquin et al., 1999;Balkanski et al., 2007). A main factor in accurately determining the sign of radiative forcing is the inclusion of absorbing dust components. Iron oxides have large imaginary portions of their complex refractive indices (http://www.atm.ox.ac.uk/project/RI/hematite.html, cited as personal communication with A.H.M.J. Triaud). Since the imaginary part of refractive indices correspond to absorption, iron oxide refractive indices control the amplitude of dust absorption in the solar and visible wavelengths (Sokolik and Toon, 1999;Claquin et al., 1999;Moosmüller et al., 2012). Efforts to separate the components of absorbing dust single out the iron oxides, hematite and goethite.

Recent modeling studies that consider the speciation of dust into its mineral components include work by Balkanski et al., 2007, Sokolik and Toon, 1999, and Nickovic et al., 2012. Balkanski reports good agreement with satellite and AERONET data (Holben et al., 1998;Holben et al., 2001) when a 1.5% internally mixed volume

weighted percent of hematite is modeled, and reports top of atmosphere (TOA) and surface forcings between -0.47 to -0.24 Wm^{-2} and -0.81 to -1.13 Wm^{-2} respectively. Sokolik and Toon investigate the optical properties of a mixture of individual minerals and of mixtures where hematite is aggregated with other minerals. They find a net negative radiative forcing for externally mixed minerals and a net positive forcing when either hematite concentrations are unrealistically high or when it is aggregated with quartz. Nickovic et al. 2012 presents high resolution mineral maps based on Claquin et al. 1999 mineral maps.

This study addresses the direct radiative forcing (DRF) of natural mineral aerosols in the Community Earth System Model. The global model simulations attempt to match the sign and magnitude of regional observations of DRF using two different atmosphere models. Dust in the Community Atmosphere Model 4, hereafter CAM4, was speciated into eight minerals, illite, kaolinite, montmorillonite, hematite, quartz, calcite, gypsum and feldspar, (Claquin et al., 1999) where the minerals along with other aerosols are treated as external mixtures (Mahowald et al., 2006). The Community Atmosphere Model 5, CAM5, treats aerosols as internal mixtures within each of three modes (Liu et al., 2011). Dust in CAM5 was speciated into four minerals, the major clays (illite, kaolinite and montmorillonite) and hematite, along with an additional tracer to carry the rest of the dust. The main objective of this work was to build the framework to model dust as its individual mineral components and to test the accuracy of emission, advection and deposition of the mineral tracers by comparing with observations from literature. An additional objective was to determine the radiative effect of speciating dust into minerals on the Earth System. Furthermore, the use of two different atmosphere models allows us to test the sensitivity of mineral speciation within different frameworks. The framework for carrying extra tracers performs reasonably well and is currently being used to

investigate elemental distributions (Zhang et al., in prep) and also cloud and ice nucleation as a function of different clay species.

The sections are organized as follows: section 2 describes methods including a description of the CESM and CAM4 and CAM5 methods for dust entrainment, transport and deposition as well as the radiation schemes used to compute global estimates of DRF. Section 3 describes the resulting mineral distributions and compares them with observations, provides a comparison of modeled optical depths and single scattering albedo to the AErosol RObotic NETwork (AERONET) ground based sun photometers (Holben et al., 1998;Holben et al., 2001) as well as global and regional estimates of radiative forcing for both CAM4 and CAM5. Also, we present a sensitivity study on dust size distribution to illustrate the significance of including mineralogy and attempt to quantify the uncertainties associated with the radiative forcing from minerals. The last section discusses the strengths of this framework and outlines where additional work is needed. Future improvements to these models will be presented along with planned future simulations of trace nutrient biogeochemical cycling with this framework.

CHAPTER 2

2.0 Methods

The Community Earth System Model version 1.0.3 (CESM 1.0.3) coordinated by the National Center for Atmospheric Research (NCAR) is a coupled earth system model used to simulate past, present and future climate (Hurrell et al., in press). This study uses CESM1.0.3 with modifications to CAM4 and CAM5.1 to simulate dust as distinct mineral tracers and to model radiation online to investigate the DRF of mineralogy.

2.1 Desert Dust Model

The CAM4 model configuration used for bulk aerosols contains active atmosphere, land and sea ice components, as well as a data ocean and slab glacier forced by NASA's GEOS-5 meteorology (FSDBAM) (Suarez et al., 2008;Hurrell et al., in press;Lamarque et al., 2012). Model resolution is on a 2.5° x 1.9° horizontal grid with 56 vertical levels. The model was run for three years, 2008-2010, and the 2010 simulation is used for analysis. The default configuration was altered so that radiative feedbacks were active and the radiation code was modified to compute radiation online, bypassing the need for Parallel Offline Radiative Transfer (PORT) (Conley et al., 2013). Because we use reanalysis winds, radiation does not feed back onto the meteorology. The dust model is part of a bulk aerosol model scheme with fixed bin width and sub-bin distribution described in Dust Entrainment and Deposition Model (DEAD) (Zender et al., 2003). Dust source and magnitude have been optimized from the default configuration and are described in (Mahowald et al., 2006;Albani et al., submitted).

Dust entrainment is initiated after the land model calculates theshhold wind velocity from surface roughness and soil moisture; dust is entrained when the wind

velocity exceeds the threshold wind velocity required for saltation (Zender et al., 2003). The threshold velocity for dust entrainment increases with increasing soil moisture and has been optimized empirically from the traditional dependence of the square of clay mass fraction (Fecan et al., 1999;Zender et al., 2003). Regions of dust emission are parameterized as being associated with topographical depressions where sedimentation from hydrological systems accumulates (Ginoux et al., 2001;Yoshioka et al., 2007;Mahowald et al., 2006;Zender et al., 2003). Particle size distributions are computed from the mass fraction of an analytic trimodal lognormal probability density function representing three source modes to four discrete sink or transport bins by Equation 1 (Zender et al., 2003)

$$M_{i,j} = \frac{1}{2}\left[\mathrm{erf}\left(\frac{\ln\left(D_{max,j}/\overline{D_{v,J}}\right)}{\sqrt{2}\ln\left(\sigma_{g,i}\right)}\right) - \mathrm{erf}\left(\frac{\ln\left(D_{min,j}/\overline{D_{v,J}}\right)}{\sqrt{2}\ln\left(\sigma_{g,i}\right)}\right)\right], \quad (1)$$

where erf is the error function (Seinfeld and Pandis, 1998), D_{max} and D_{min} correspond to the transport bins bounded at diameters 0.1, 1.0, 2.5, 5.0 and 10.0μm with a sub-bin lognormal distribution with mass median diameter, $\overline{D_v}$, of 3.5μm and geometric standard deviation, σ_g = 2 (Reid et al., 2003;Mahowald et al., 2006;Zender et al., 2003). Particle size distributions were modified (default mass fractions are 3.8, 11,17 and 67% for size bins 1-4) following brittle fragmentation theory for vertical dust flux (Kok, 2011), with prescribed mass fractions in each bin of 1.1, 8.7, 27.7 and 62.5% respectively. Dry deposition includes gravitational settling and turbulent deposition and wet deposition includes scavenging (Rasch et al., 2000;Zender et al., 2003;Mahowald et al., 2006). The scavenging coefficients and particle solubility parameterizations were modified from (0.1, 0.1 bins 3 and 4) to (0.3, 0.3 for bins 3 and

4), and the prescribed solubility was changed from 0.15 to 0.3 (Albani et al., submitted). Leaf area index was increased from 0.1 to 0.3 m^2/m^2 following (Mahowald et al., 2006).

The CAM5 model configuration used for modal aerosols is stand-alone atmosphere with land and sea ice components, as well as a data ocean and slab glacier forced by model winds and CAM5 physics (FC5) (Liu et al., 2011). Model resolution is on a 2.5° x 1.9° horizontal grid with 30 vertical levels. The model was run for three years using anthropogenic emissions from the year 2000, and the third year is used for analysis. Radiative feedbacks were active and allowed to feed back onto meteorology. Dust entrainment processes are identical to the release version of CAM4 with the exception of an increase in the leaf area index threshold from 0.1 to 0.3 m^2/m^2 (Okin, 2008;Liu et al., 2011), which has also been applied in CAM4. The particle size distribution differs from the bulk aerosol method with lognormal functions describing the distribution via a modal aerosol model (MAM). Mass mixing and number mixing ratios within a given mode are predicted, with fixed geometric standard deviation of each mode. Aerosols and water vapor are internally mixed within a mode and externally mixed between modes with the exception of ageing of primary organic carbon from Aitken mode to accumulation mode. Dust is carried in an accumulation mode (Mode 1) and a coarse mode (Mode 3) with diameter bounds at 0.1–1.0μm and 1.0-10.0μm, respectively. The particle size distribution for dust entrainment was modified (default mass percents are 3.2 and 96.8% for modes 1 and 3, respectively) following brittle fragmentation theory for vertical dust flux (Kok, 2011) with prescribed emission mass percents of 1.1 and 98.9% for modes 1 and 3. Advection and deposition processes are described in Liu et al. 2011, where aerosols are represented as both interstitial particles suspended in the atmosphere and as cloud-borne particles.

Table 1: Mean Mineralogical Table from Claquin et al. 1999. Gypsic xerosols and yermosols (Xy,Yy), Gleyic Solontchaks, (Zg), Orthic Solontchaks (Zo) and salt flats (ST) are renormalized to 100. Hematite is added to the clay fraction by subtracting the mass from Illite following Balkanski et al., 2007.

	Clay Fraction						Silt Fraction				
Soil Types	Ill	Kaol	Sme	Cal	Quar	Hem	Quar	Feld	Cal	Hem	Gyp
I	39	20	29	4	7	1	52	40	6	1	1
Jc	22	9	46	11	12	0	30	38	29	0	2
Je	17	23	55	1	3	1	86	10	2	1	1
Qa	20	54	21	0	4	1	83	15	0	1	1
Qc	12	67	5	1	11	4	80	14	1	4	1
Qf	22	48	23	1	5	1	82	15	1	1	1
Ql	3	77	3	1	9	7	69	22	1	7	1
Rc	39	39	9	4	7	3	74	19	3	3	1
Re	30	52	10	1	5	2	58	38	1	2	1
So	35	32	17	6	7	2	70	23	4	2	1
Vc	12	27	48	4	5	4	31	61	3	4	1
Xh	18	54	22	1	3	2	72	24	1	2	1
Xk,Yk	55	13	16	11	3	2	76	7	14	2	1
Xl,Yl	43	20	20	7	7	2	69	23	5	2	1
Xt	20	50	21	3	5	1	16	78	4	1	1
Xy,Yy	27	18	40	8	7	0	54	25	15	0	6
Zg	16	33	24	21	5	0	45	25	18	0	13
Zo	30	6	46	11	7	1	32	41	21	1	6
Zt	25	33	25	10	6	0	22	65	12	0	1
SD	49	9	26	1	14	1	91	6	1	1	1
ST	39	4	26	29	1	1	4	1	74	1	21

Source maps of minerals follow the mean mineralogical table (MMT) from (Claquin et al., 1999), with two modifications. From the MMT, soil types whose mineral components found not to add up to 100% were gypsic xerosols and yermosols, gleyic and orthic solontchaks and salt flats (Table 1). In addition to renormalizing the soil types, hematite was added to the clay fraction (0-2µm) with the same proportion

as prescribed in the silt fraction (2-50μm) by subtracting the required fraction from illite (Balkanski et al., 2007).

Mineralogy was mapped on FAO/UNESCO WGB84 at 5' x 5' arc minutes with soil legend from FAO/UNESCO Soil Map of the World (1976; File Identifier: f7ccd330-bdce-11db-a0f6-000d939bc5d8) (Batjes, 1997). The corresponding mineral maps were regridded to model resolution (2.5° x 1.9°) (Figure 1). A nearest neighbor algorithm was applied to estimate mineralogy of land mass not specified by the soils in Claquin's MMT to allow non-zero dust emissions in these regions. The clay-sized soils (0-2μm) and silt-sized soils (2-50μm) are distributed in the four CAM4 bins and two CAM5 modes following brittle fragmentation theory (Kok, 2011) (Table 2). Details following this conversion are described in the following sub-section.

Table 2a: The fraction of dust aerosol mass contributed by the soil clay and silt fractions for each of the 4 particle size bins for the bulk scheme in CAM4 from work by Kok 2011.

Particle size bin	Lower bin limit D_p (μm)	Upper bin limit D_p (μm)	Fraction of aerosol mass from soil clay fraction	Fraction of aerosol mass from soil silt fraction
1	0.1	1	1	0
2	1	2.5	0.970	0.030
3	2.5	5	0.625	0.375
4	5	10	0.429	0.571

Table 2b: The fraction of dust aerosol mass contributed by the soil clay and silt fractions for each of the 2 particle modes for the modal scheme in CAM5 from work by Kok 2011.

Particle mode	Lower bin limit D_p (μm)	Upper bin limit D_p (μm)	Fraction of aerosol mass from soil clay fraction	Fraction of aerosol mass from soil silt fraction

1	0.1	1	1	0
2	1	10	0.695	0.305

2.2 Conversion of Soil Mineralogy to Aerosol Mineralogy

The conversion of soil mineralogy to dust aerosol mineralogy for a given transport particle size bin follows brittle fragmentation theory (Kok, 2011) of dust emission where the production of dust aerosols with size D_d is proportional to the volume fraction of soil particles with size $D_s \leq D_d$ according to Equation 2,

$$\frac{dV_d}{dD_d} \propto \int_0^{D_d} P_s(D_s) dD_s \tag{2}$$

where V_d is the normalized volume of dust aerosols with size D_d and $P_s(D_s)$ is the particle size distribution of fully disaggregated soil particles. For a mineralogy data set with clay (0-2 μm diameter) and silt (2-50 μm diameter) soil fractions, we use Equation 2 to convert from soil mineralogy to dust aerosol mineralogy. More specifically, for a given aerosol with size D_d the mass fraction originating from the soil clay and silt particle fractions are given by Equation 3a and 3b respectively,

$$f_{clay}(D_d) = \int_0^{D_{clay}} P_s(D_s) dD_s \Big/ \int_0^{D_d} P_s(D_s) dD_s \,, \tag{3a}$$

$$f_{silt}(D_d) = \int_{D_{clay}}^{D_d} P_s(D_s) dD_s \Big/ \int_0^{D_d} P_s(D_s) dD_s \tag{3b}$$

where D_{clay} = 2 μm and $f_{clay} + f_{silt} = 1$, and $D_d > D_{clay}$. When $D_d < D_{clay}$, $f_{clay} = 1$ and $f_{silt} = 0$. The integrals in (Equation 3a,3b) are evaluated by assuming that the soil

particle size distribution follows a log-normal distribution (Kolmogorov, 1941) according to Equation 4,

$$P_s(D_s) = \frac{1}{D_s\sqrt{2\pi}\ln(\sigma_s)}\exp\left\{-\frac{\ln^2(D_s/\overline{D_s})}{2\ln^2(\sigma_s)}\right\} \quad (4)$$

where $\overline{D_s}$ is the median diameter by volume and σ_s is the geometric standard deviation. Measurements of the particle size distribution of arid soil indicate that $\overline{D_s} \approx 3.4$ μm and $\sigma_s \approx 3.0$ for soil distributions less than 20 μm (Kok, 2011). Combining Equations 3 and 4 yields Equation 5a and 5b,

$$f_{clay}(D_d) = \frac{1 + \mathrm{erf}\left[\frac{\ln(D_{clay}/\overline{D_s})}{\sqrt{2}\ln(\sigma_s)}\right]}{1 + \mathrm{erf}\left[\frac{\ln(D_d/\overline{D_s})}{\sqrt{2}\ln(\sigma_s)}\right]}, \quad (5a)$$

$$f_{silt}(D_d) = \frac{\mathrm{erf}\left[\frac{\ln(D_d/\overline{D_s})}{\sqrt{2}\ln(\sigma_s)}\right] - \mathrm{erf}\left[\frac{\ln(D_{clay}/\overline{D_s})}{\sqrt{2}\ln(\sigma_s)}\right]}{1 + \mathrm{erf}\left[\frac{\ln(D_d/\overline{D_s})}{\sqrt{2}\ln(\sigma_s)}\right]} \quad (5b)$$

To obtain the fraction of dust aerosol mass from the soil clay and silt fraction for a given particle size bin, Equation 5a,b are integrated over the bin's size boundaries and weighted by the sub-bin distribution following Equation 6a and 6b,

$$f_{clay,bin} = \int_{D_-}^{D_+} f_{clay}(D_d)\frac{dV}{dD_d}dD_d \Big/ \int_{D_-}^{D_+} \frac{dV}{dD_d}dD_d \quad (6a)$$

$$f_{silt,bin} = \int_{D_-}^{D_+} f_{silt}(D_d)\frac{dV}{dD_d}dD_d \Big/ \int_{D_-}^{D_+} \frac{dV}{dD_d}dD_d \quad (6b)$$

where D_- and D_+ are the lower and upper size limits and dV/dD_d is the sub-bin dust size distribution by volume. As previously stated, the sub-bin size distribution in CAM follows a log-normal distribution with mass median diameter of 3.5 μm and geometric standard deviation of 2.0 (Zender et al., 2003;Reid et al., 2003).

2.3 Modeling of Radiation

Radiation in CAM4 is parameterized using the delta-eddington approximation (Joseph et al., 1976;Coakley Jr et al., 1983) to determine the reflectivity and transmissivity for each of 19 shortwave spectral intervals at each vertical layer in the atmosphere. The vertical layers are combined and the upward and downward flux between layers is computed once per model hour. The optical properties for each aerosol species including extinction and single scattering albedo in SW are calculated offline from species refractive indices with a Mie solver (Wiscombe, 1980). The mineral species whose SW optical properties have been derived from their respective refractive indices are illite, kaolinite, montmorillonite, hematite and feldspar (Table 3) with the remaining mineral species, quartz, gypsum and calcite being represented by a "rest of dust" blend with optics calculated with Maxwell-Garnett mixing of 48% quartz, 25% illite, 25% montmorillonite and 2% calcite by volume. The density of each mineral is explicitly included (ρ_{illite} = 2750 kg/m^3, $\rho_{kaolinite}$ = 2600 kg/m^3, $\rho_{montmorillonite}$ = 2350 kg/m^3, ρ_{quartz} = 2660 kg/m^3, $\rho_{calcite}$ = 2710 kg/m^3, $\rho_{hematite}$ = 5260 kg/m^3, $\rho_{feldspar}$ = 2560 kg/m^3, ρ_{gypsum} = 2300 kg/m^3), while the density of the "rest of dust" blend is 2500 kgm^{-3}. Hygroscopicity for all minerals as well as the dust blend is prescribed at 0.068; different mineral species have unique water uptake ability and thus different hygroscopicities. This leads to different CCN or IN capabilities but was beyond the scope of this study. Not all the mineral species were modeled optically for several reasons. Refractive indices for all eight minerals were not readily available at solar

wavelengths (SW), nor was a solver to generate optical properties at infrared wavelengths (LW). In place of LW optical properties for the minerals, CAM3 optics were used (Mahowald et al., 2006), which were computed assuming Maxwell-Garnett mixing of 47.6 % quartz, 25% illite, 25% montmorillonite, 2% calcite and 0.4% hematite by volume, with density = 2500 kg/m^3 and hygroscopicity prescribed as 0.14.

Table 3: Refractive indices of minerals used , wavelengths of refractive indices and references for input into CAM4 and CAM5. Refractive indices specified as Zender are a Maxwell-Garnet internal mixture of 48% quartz, 25% illite, 25% montmorillonite and 2% calcite by volume. These were used primarily to simplify the comparison of CAM4 and CAM5. Longwave optics for CAM4 were taken from CAM3 because a solver was not available to calculate the absorption coefficients.

Minerals	Refractive Indices	Wavelengths	CAM4	CAM5
Illite	Egan and Hilgeman 1979	0.19 to 2.5 µm	X	X
	Querry 1987	2.5 to 50.0 µm	X	X
Kaolinite	Egan and Hilgeman 1979	0.19 to 2.5 µm	X	X
	Querry 1987	2.5 to 50.0 µm	X	X
Montmorillonite	Egan and Hilgeman 1979	0.19 to 2.5 µm	X	X
	Querry 1987	2.5 to 50.0 µm	X	X
Quartz	Zender	0.2 to 40.0 µm	X	
Calcite	Zender	0.2 to 40.0 µm	X	
Hematite	A.H.M.J. Triaud	0.1 to 40.7 µm	X	X
Feldspar	Egan and Hilgeman 1979	0.19 to 2.5 µm	X	
	Zender	2.5 to 40.0 µm	X	
Gypsum	Zender	0.2 to 40.0 µm	X	
Dust-Other	Zender	0.2 to 40.0 µm		X

Radiation in CAM5.1 is parameterized with Rapid Radiative Transfer Model for GCM (RRTMG) (Liu et al., 2011;Iacono et al., 2008) with 14 and 16 spectral bands in SW and LW respectively. Mineral optical properties are parameterized by wet refractive index and wet surface mode radius (Ghan and Zaveri, 2007). Since this parameterization only utilizes refractive indices, the LW absorption parameters were generated. Flux calculations are done once per model hour for shortwave and longwave flux during model day ($\cos(\theta_0) > 0$).

The direct radiative forcing from dust for all simulations is determined by calculating the radiative forcing twice at each time step, one time through with all aerosol species and an additional time through with everything but dust or minerals. Both atmosphere models only account for absorption in LW for mineral aerosols, which may underestimate radiative forcing by up to 20%.

CAM5 was modified to include five mineral tracers, 4 minerals and an additional tracer to carry the rest of dust; neglecting the radiative properties of the additional minerals in CAM4 facilitated a comparison between models. The fewer tracers in CAM5 were simply for computational efficiency; the capability to add the additional minerals included in CAM4 is feasible and future simulations may involve including these.

2.4 Description of Simulations

The cases simulated for both CAM4 and CAM5 are listed in Table 4. CAM4-t and CAM5-t simulations consist of a variety of optimizations to better simulate observed dust emission, transport, depositional fluxes and optical properties. The tuning consists of optimized soil erodibility maps for each model (Mahowald et al., 2006;Albani et al., submitted), emission particle size distribution following brittle fragmentation theory (Kok, 2011), increased solubility for dust, increased cloud

scavenging coefficients (Albani et al., submitted) and improved optical properties including extinction, scattering and absorption coefficients derived from the refractive indices from Maxwell-Garnett mixing of 47.6% quartz, 0.4% hematite, 25% illite, 25% montmorillonite and 2% calcite by volume, with density = 2500 $kgm^{-3}$and hygroscopicity = 0.068.

Table 4: Description of the model simulations used in this study. All cases are for three years with the third year used for comparisons to observations and for RF calculations. All cases are run at 1.9°x2.5° resolution. FSDBAM indicates bulk aerosols, active atmosphere, land and sea ice components, data ocean, slab glacier and GEOS5 meteorology. FC5 indicates modal aerosols, stand-alone atmosphere with land and sea ice components, data ocean, slab glacier, model winds and CAM5 physics.

Case	Configuration	Emission Size Distribution	Optics
CAM4-t	FSDBAM	Kok et al. 2011	tuned
CAM4-m	FSDBAM	Kok et al. 2011	Table 3
CAM5-t	FC5	Kok et al. 2011	tuned
CAM5-m	FC5	Kok et al. 2011	Table 3
CAM4-trs	FSDBAM	release	tuned
CAM5-trs	FC5	release	tuned

CAM4-m and CAM5-m simulations employ the same tuning parameterizations as the tuned cases except the optical properties (extinction, scattering, absorption) are derived from the mineral refractive indices (Table 3), and the emissions are scaled by the mineral maps described in section 2.1,2.2. A sensitivity study is also undertaken in order to quantify the importance of including mineralogy in place of dust in a global model for RF calculations, in contrast to size distribution. The tuning

parameterizations for dust in both CAM4 and CAM5 are kept constant except the new size distribution was replaced with the size distribution in the release version of the model with mass fractions of 0.038, 0.11, 0.17 and 0.67 for bins 1-4 (CAM4-trs) and mass fractions 0.032 and 0.968 for modes 1 and 3 (CAM5-trs).

2.5 Comparison to Observations

The following sections describe the comparison of mineralogy to in situ field measurements as well as ocean core sediment data (Table 5). Distinguishing natural mineral aerosol is complicated by atmospheric mixing with anthropogenic aerosols and other natural aerosols, as well as the distance between the dust source and the location of the observations (Claquin et al., 1999;Kalashnikova and Kahn, 2008). Additionally, ocean sediment measurements are complicated by complex ocean circulation patterns (Han et al., 2008;Siegel and Deuser, 1997). A wide variety of methods are used for dust sample collection; this can impact measuring concentrations of smaller or highly aspherical particles (Reid et al., 2003), the non-uniformity of which further complicates the model verification process. As a way to compare observed mineralogy where particle size distribution is not explicitly reported, and to avoid the different methods of defining size basis (Glaccum and Prospero, 1980;Biscaye, 1965), the mass ratio of minerals with similar diameters are compared to the mass ratios of observed mineralogy (Claquin et al., 1999).

Table 5: Observations of mineralogy used to evaluate simulated mineral distributions in CAM4 and CAM5. Data that is suspended near the surface was chosen in order to compare to dry deposition in the models. Ocean core sediment data is compared to bulk dry and wet deposition.

Reference	Location	Type of Data	Month	Type
Biscaye 1965	Atlantic Ocean	Sediment	N/A	K/I
Cacquineau et al. 1998	Tropical N. Atlantic	Suspended (< 20 m) Ratio	April	K/I

Engelbrecht et al. 2009b	Middle East	Suspended (< 20 m)	Annual	H/Q; C/Q; F/Q; H/I
Falkovich et al. 2001	Isreal	Suspended (< 20 m) Ratio	March	K/I; C/Q; F/Q
Glaccum and Prospero 1980	Tropical N. Atlantic	Suspended (< 20 m) Ratio	Aug.	K/I; C/Q; F/Q
Kandler et al. 2009	Morocco	Suspended (< 20 m) Ratio, Volume Fraction	May	K/I; H/I; C/Q; F/Q; H/Q; I,K,Q,C,H,F,G
Kiefert et al. 1996	Charleville, AUS	Suspended (< 20 m) Ratio	Dec.	K/I
Prospero and Bonatti 1969	Equitorial Pacific	Suspended (< 20 m) Ratio	FMA	K/I; F/Q
Shen et al. 2005	N. China	Suspended (< 20 m) Ratio	MAM	K/I
Shi et al. 2005	Beijing	Suspended (< 20 m) Ratio	March	C/Q; F/Q; H/Q

Dry deposition of minerals in CAM4 and CAM5 is compared to one available observation (Kandler et al., 2009) of relative mineral volume abundance as a function of mean particle diameter (Figure 4). Following conversion to relative mass fractions, the average mass abundance for CAM4 bin1 was correlated to particle diameters 0.16, 0.35 and 0.71μm according to Equations 7 and 8,

$$\bar{\gamma}\rho = \frac{\int_{0.1}^{D_{1,+}} \frac{dV}{dD}\gamma_1 dD + \int_{D_{2,-}}^{D_{2,+}} \frac{dV}{dD}\gamma_2 dD + \int_{D_{3,-}}^{1} \frac{dV}{dD}\gamma_3 dD}{\int_{0.1}^{1} \frac{dV}{dD} dD} \quad (7)$$

Where

$$\frac{dV_d}{dD_d} = \frac{1}{c_v}\left[1 + \mathrm{erf}\left(\frac{\ln\left(D_d/\overline{D_s}\right)}{\sqrt{2}\ln\left(\sigma_s\right)}\right)\right]\exp\left[-\left(\frac{D_d}{\lambda}\right)^3\right] \quad (8)$$

$D_{1,+} = D_{2,-} = 0.24$ μm, $D_{2,+} = D_{3,-} = 0.5$ μm. V_d is the normalized volume of dust aerosols with size D_d, $c_v = 12.62$ μm is a normalization constant. Equation 8 is the predicted size distribution at emission following brittle fragmentation theory (Kok, 2011). The size distribution at emission and the distribution observed for particles of diameters < 1.0μm are expected to be similar given the proximity of the measurements to the emission source as well as the negligible impact of gravitational settling. Particle diameters 1.6, 3.5 and 7.1μm correspond well with bins 2-4, respectively. For CAM5, the accumulation mode was matched with the correlation for bin 1 and the coarse mode average mass fraction of mineral species was estimated by estimated by Equation 9

$$\frac{dV_d}{dD_d} = \left[0.5 + 0.5\mathrm{erf}\left(\frac{\ln\left(D_d/\overline{D_{pg}}\right)}{\sqrt{2}\ln\left(\sigma_g\right)}\right)\right], \tag{9}$$

the size distribution at emission, and Equation 10,

$$\bar{\gamma} * \rho = \frac{\int_1^{D_{1,+}} \frac{dV}{dD}\gamma_1 dD + \int_{D_{2,-}}^{D_{2,+}} \frac{dV}{dD}\gamma_2 dD + \int_{D_{3,-}}^{D_{3+}} \gamma_3 dD + \int_{D_{4,-}}^{10} \gamma_4 dD}{\int_1^{10} \frac{dV}{dD} dD} \tag{10}$$

Comparing the modeled distribution of minerals with observations that do not specify the particle size distribution is not very effective since there is a correlation between mineralogy for a given particle size distribution (Claquin et al., 1999). For this reason, the ratio of similarly- sized minerals are compared. The following mineral ratios were chosen because they matched the similar size criterion and had more than five locations of observation. In the clay-size range, kaolinite to illite (K/I) and hematite to illite (H/I) are chosen because comparisons were possible for both CAM4 and CAM5. In the silt-size range, the following comparisons were made: calcite to

quartz (C/Q), feldspar to quartz (F/Q), and hematite to quartz (H/Q). Note that hematite is treated in both fine and coarse modes as the particle size distribution of hematite may differ from the (Claquin et al., 1999) MMT case where hematite was prescribed solely in the coarse mode. While it was acknowledged that the available data on hematite was very limited, recent observations suggest that hematite is predominantly in the smaller, clay-sized range. (Cwiertny et al., 2008) finds much higher relative iron concentrations in particles < 0.75μm diameter. Higher iron concentrations indicate iron rich oxides/hydroxides as opposed to iron substitutions in silicate clay lattices, which are typically quite small (Journet et al., 2008).

CHAPTER 3

3.0 RESULTS

3.1 Desert Dust Mineralogical Distribution

The spatial distribution of minerals in CAM4 and CAM5 are different (Figure 2 and 3) and likely follow from the distribution of minerals in soils (Figure 1) and the disparate meteorology: reanalysis meteorology in CAM4 versus the model winds in CAM5. In order to discuss the significance of the spatial distribution of mineralogy and to give credibility to the simulations, the modeled distributions are evaluated with available observational data (Table 5).

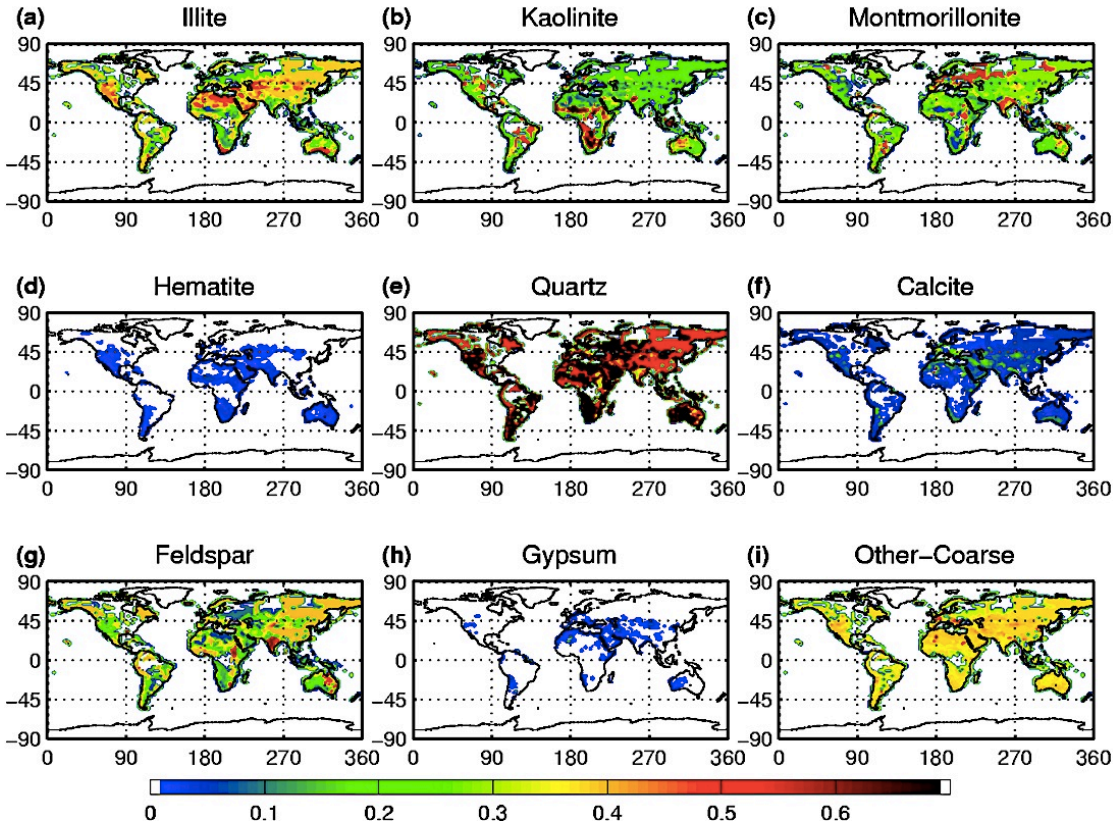

Figure 1: Mineral fraction maps for CAM4 and CAM5 based on work by Claquin et al. (1999). Illite (a), Kaolinite (b), Montmorillonite (c) are clay-sized (0-2μm). Hematite (d) has the same distribution for both clay-sized and silt-sized (2-20μm). Quartz (e), Calcite (f), Feldspar (g), Gypsum (h) and Other-coarse (i) silt-sized. CAM4 includes Illite (a), Kaolinite (b), Montmorillonite (c), Hematite (d), Quartz (e), Calcite (f), Feldspar (g), and Gypsum (h). CAM5 includes Illite (a), Kaolinite (b), Montmorillonite (c), Hematite (d) and Other-Coarse (i) which represents quartz, calcite, feldspar, and gypsum.

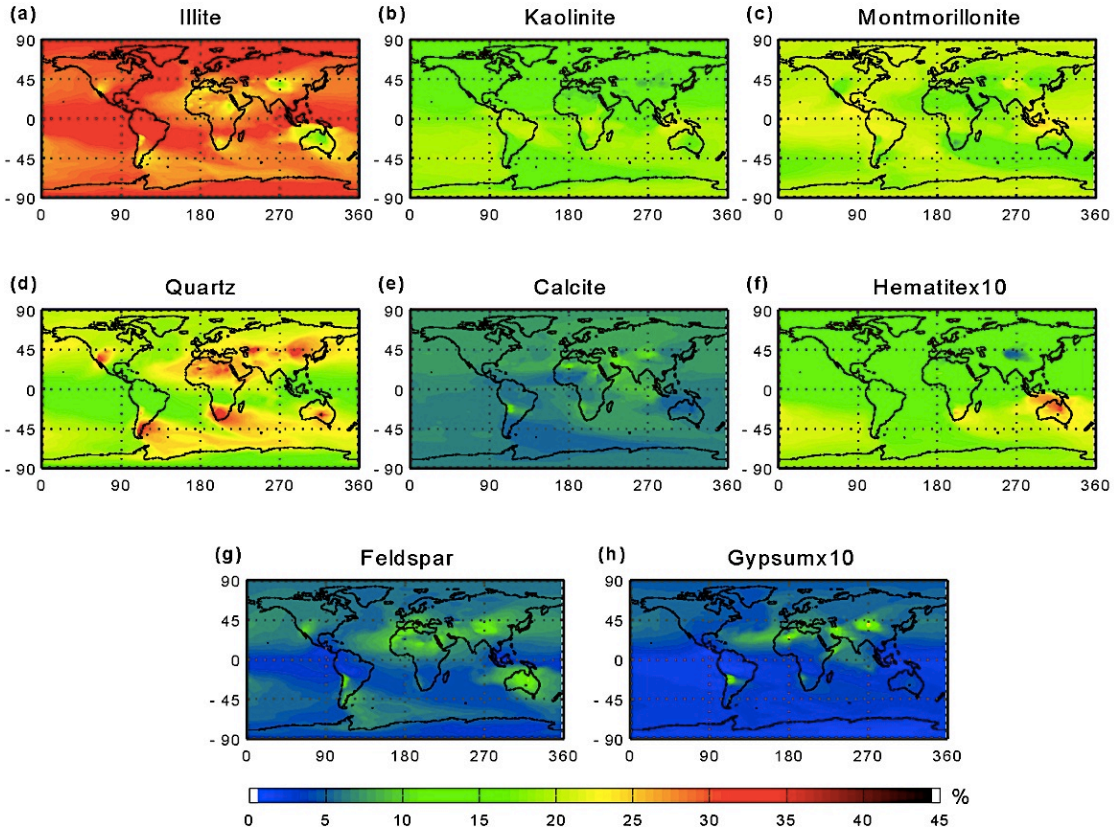

Figure 2: Total percent column mineral distributions for CAM4 shown as the sum of all four bins for each mineral. Hematite (f) and Gypsum (h) are scaled by 10 so that they can be visually compared with Illite (a), Kaolinite (b), Montmorillonite (c), Quartz (d), Calcite (e) and Feldspar (g).

Because of the size segregation of the minerals in the soil materials (Claquin et al., 1999), it is ideal to compare the modeled mineralogy by size distribution. However, there is limited size segregated data (Table 5; Figure 4). For four of the seven minerals considered—illite (Figure 4a), kaolinite (Figure 4b), quartz (Figure 4c) and feldspar (Figure 4f)—the simulations for both CAM4 and CAM5 simulate dynamic range in mineral mass fraction with particle size, while the mass fractions observed are relatively constant with size. This is because we assumed that the clay sized minerals dominate the smaller size bins while the silt sized minerals dominate the larger size bins.

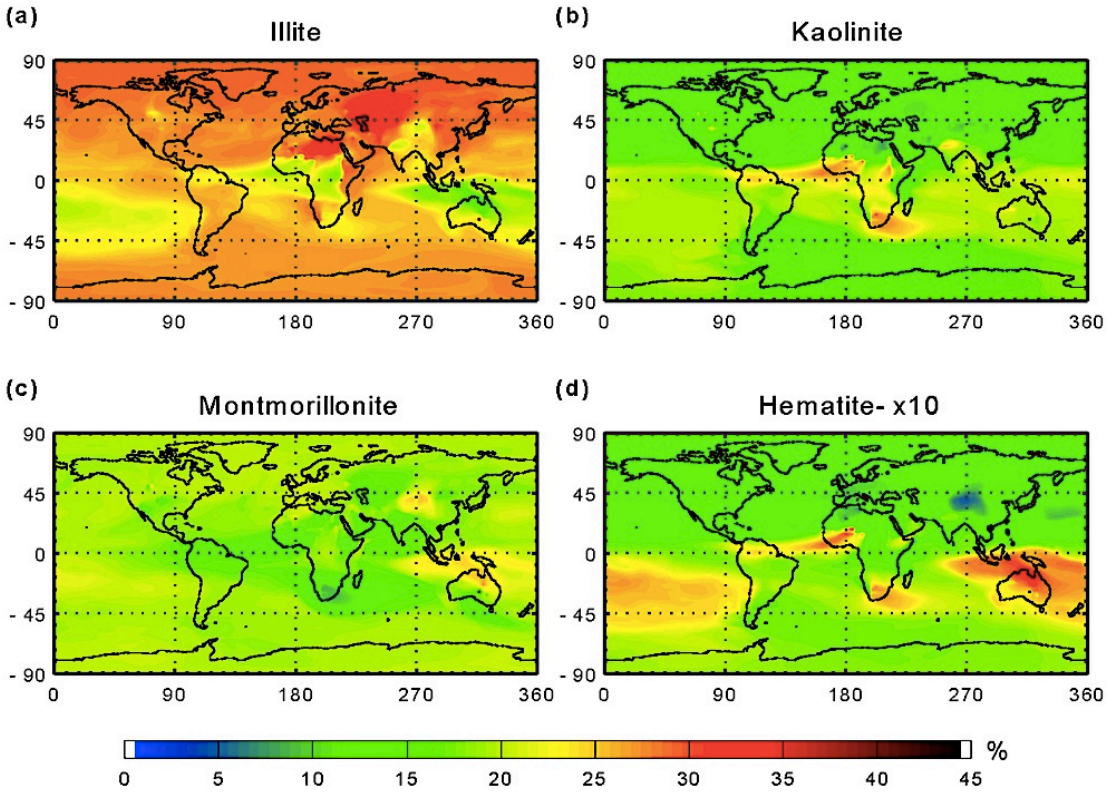

Figure 3: Total percent column mineral distributions for CAM5 shown as the sum of the fine mode (mode 1) and coarse mode (mode 3) for each mineral. Hematite (d) is scaled by 10 so that it can be visually compared with Illite (a), Kaolinite (b) and Montmorillonite (c).

While the magnitude of dry deposition velocities for any given mineral is larger in the coarser bins, the relative mass for finer bins (1 and 2) is dominated by clay minerals and the relative mass for coarser bins (3 and 4) is dominated by silt-sized minerals. The proximity of the observation to the source of emission along with the fact that samples are daily averages (rather than over a month) is another reason why the relative fractions sampled are constant with size, since transport and deposition haven't significantly altered the mineral distributions at emission, while the timescale in the observations does not necessarily reflect the simulation climatological timescale of monthly averages. There is one instance of the dynamic variability of mass with size where the CAM4 simulation did not predict this variability for gypsum (Figure 4g).

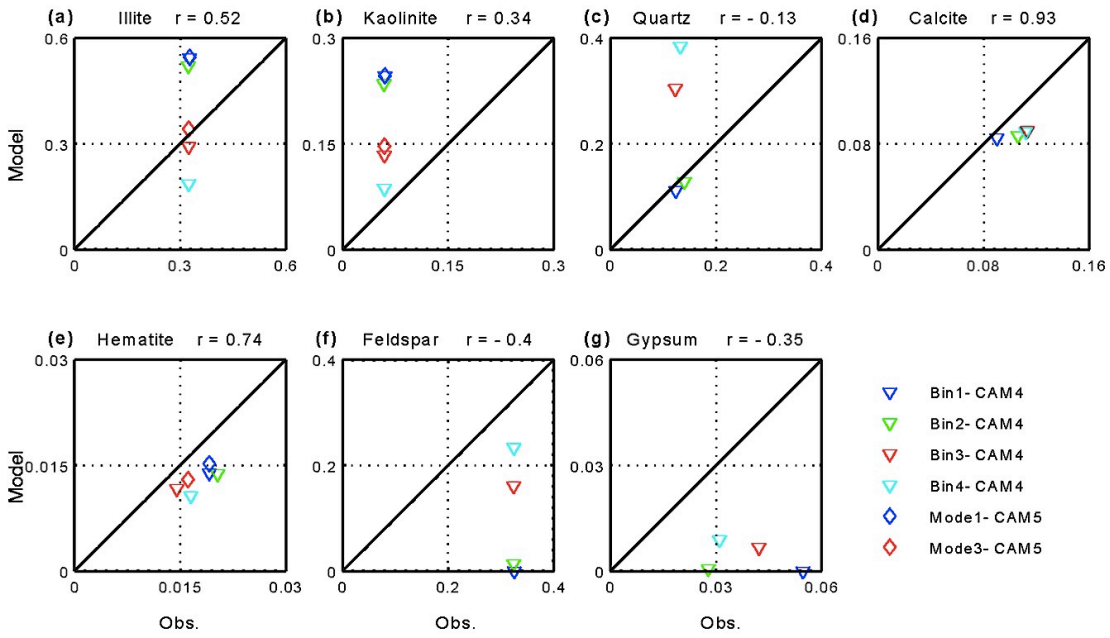

Figure 4: Relative mass abundance of minerals as modeled compared to observations from Kandler et al. (2009) for CAM4, bins 1-4, and CAM5, mode 1 and mode 3. The CAM4 comparison is for Quartz (c), Calcite (d), Feldspar (f) and Gypsum (g). Comparisons for CAM4 and CAM5 include Illite (a), Kaolinite (b) and Hematite (e).

In general, gypsum concentrations predicted from Claquin's MMT were very small (Figure 1h, Figure 2h) and this may cause a low bias in the model. However, Glaccum and Prospero (1980) reported gypsum crystallizing on collection plates and was hence not considered to have been part of the transported minerals observed during their field study. Given the discrepancies on how to measure gypsum concentrations along with atmospheric processing of gypsum (Glaccum and Prospero, 1980) that was not simulated in this study, the attempt to correlate gypsum observations with simulated gypsum concentrations is likely not very meaningful. Calcite, (Figure 4d), and hematite, (Figure 4e), are statistically significant and correlate with observations at this location, with hematite being most important for simulating the DRF in the shortwave, which is one of the primary goals of this study.

Next we compare the ratio of minerals available in the observations (Table 5). In general, both CAM4 and CAM5 do not capture the dynamic range seen in the observations (Figures 5-8). K/I in CAM5 indicates some structure and range in possible values; however the sites of observation are all in the N. Hemisphere, except for one site in Australia, limiting comparisons where CAM5 predicts greater range (Figure 7). The comparison of H/I (Figure 6) has far fewer observations; while the same overall "flatness" is seen in the model, CAM4 does better than CAM5, r = 0.82 and 0.54 respectively. The silt-size mineral ratios are only compared for CAM4 since quartz is not explicitly modeled in CAM5, and similarly indicate the inability of the model to capture the dynamic range of observed ratios.

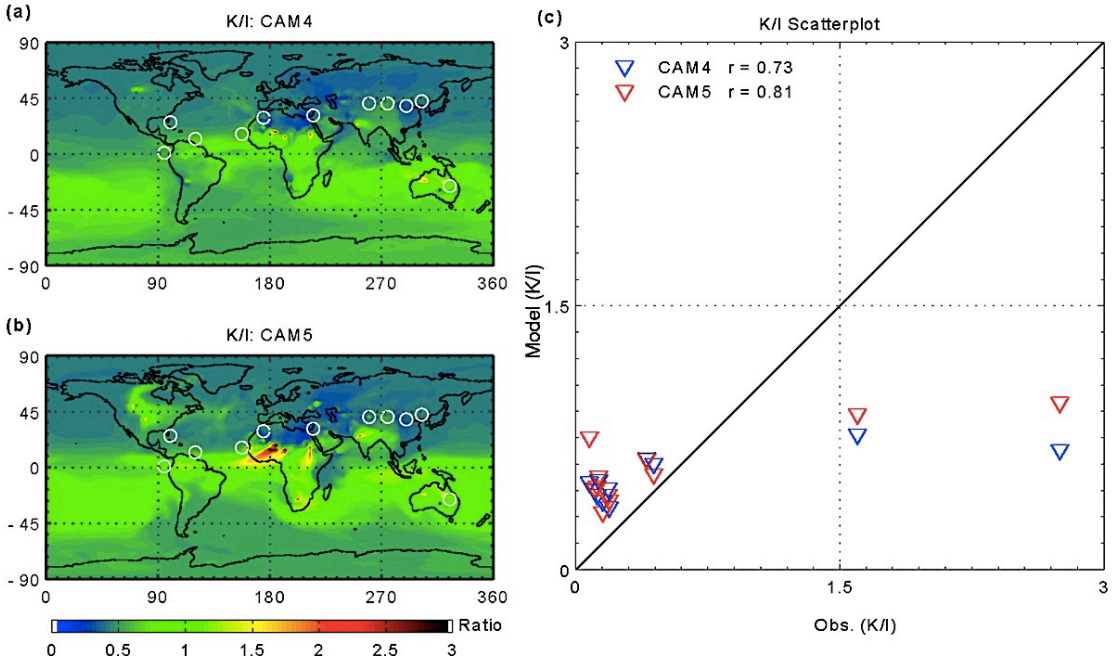

Figure 5: Kaolinite/Illite mineral ratio of bulk dry deposition from CAM4 and CAM5 (kg K/ kg I) compared to bulk observational ratios (kg K/ kg I) from field work by Shen et al. (2005), Glaccum and Prospero (1980), Kandler et al. (2009), Prospero and Bonatti (1969), Caquineau et al. (1998), Kiefert et al. (1996) and Falkovich et al. (2001).

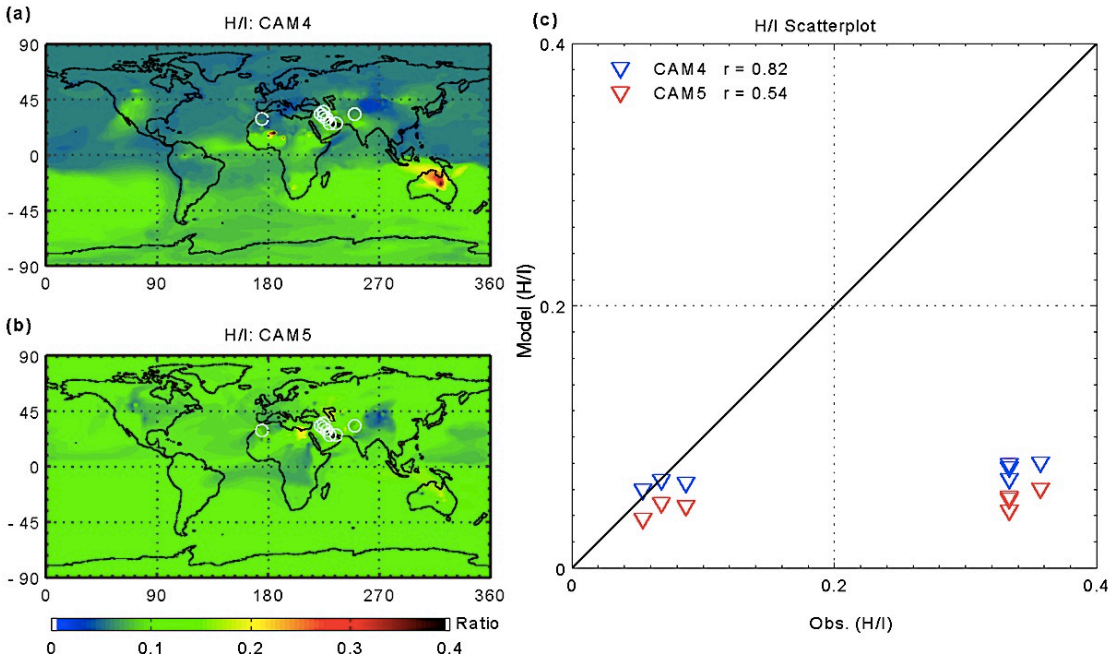

Figure 6: Hematite/Illite mineral ratio of bulk dry deposition from CAM4 and CAM5 (kg H/ kg I) compared to bulk observational ratios (kg H/ kg I) from field work by Engelbrecht et al. (2009b) and Kandler et al. (2009).

Typically, dust samples from field studies are collected during a dust event over a period of 1-3 days. The model simulations were output as monthly means and comparisons to the observations were made for the month in which they occurred. This interpretation is not ideal as the meteorological and climatological bases operate on different time scales with a greater variability expected on a daily basis. Therefore, while the simulated mineral ratios don't appear to have the dynamic variability from observations, this is likely at least partially an artifact of the smoothing effect from monthly averages.

Modeled mineral ratio K/I is compared to ocean core sediment mineralogy for CAM4 (Figure 7) and CAM5 (Figure 8) (Biscaye, 1965). The correlations for both models are quite poor overall, although the range in values for CAM5 is slightly better, with 95% of data points falling between 0.4 and 1.2, compared to CAM4 with a range of 0.4 to 1.05. Note some resemblance of the spatial pattern of Biscaye's data

(Figure 7b,8b) with CAM5 (Figure 8a) around N. Africa and eastern S. America. The latitude band correlations for CAM4 and CAM5 are poor however CAM5 appears to have more range along the equator. While these figures do not capture the range in the data, the comparison is inherently difficult given ocean circulation of dust from deposition on the surface to sedimentation on the ocean floor that the simulated deposition distributions cannot be expected to capture (Han et al., 2008;Siegel and Deuser, 1997). This along with physical and chemical processing during atmospheric transport and sedimentation further hinder the comparison.

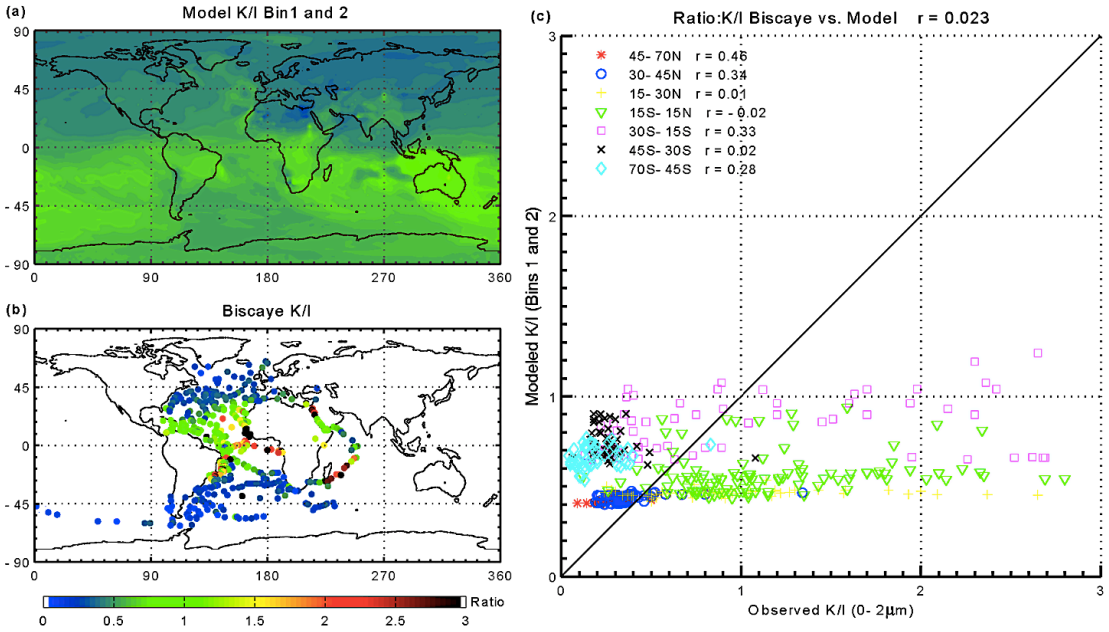

Figure 7: Kaolinite/Illite mineral ratio of wet and dry deposition for bin 1 and bin 2 from CAM4 (a) (kg K/kg I) and from characteristic basal X-ray diffraction maxima ratios of K/I of ocean core sediments (b) (Biscaye 1965). Data is segregated by latitude bands in scatterplot (c).

Summarizing the above comparisons, the mineralogical distributions simulated by the model do not have the dynamic range that the few available observations indicate. However, multiple factors are responsible, from differing time scales of observations to the atmospheric processing of dust that is not yet included in these models. As this study was a first attempt at modeling global mineralogy and was

primarily dedicated to building the framework required to carry multiple mineral tracers as well as synching them with the radiation codes, a module to simulate physical and chemical fractionation and processing of minerals during emission and transport is beyond the scope of this study. Therefore, these simulations cannot be expected to capture all the observed mineral characteristics of dust deposited away from the source. For example, observations suggest that calcite concentrations in airborne dust are a function of the wind velocity that occurred during saltation, with the relative amount decreasing with increasing velocity (Caquineau et al., 1998;Gomes et al., 1990;Sabre et al., 1997), a process that is not included here. In addition, acidic processing of calcite to gypsum would also result in less calcite abundance in collected dust and an overall increase in the abundance of clay. In the future, improvements to the simulation of the distribution of mineralogy, especially to better capture the dynamic range, are necessary.

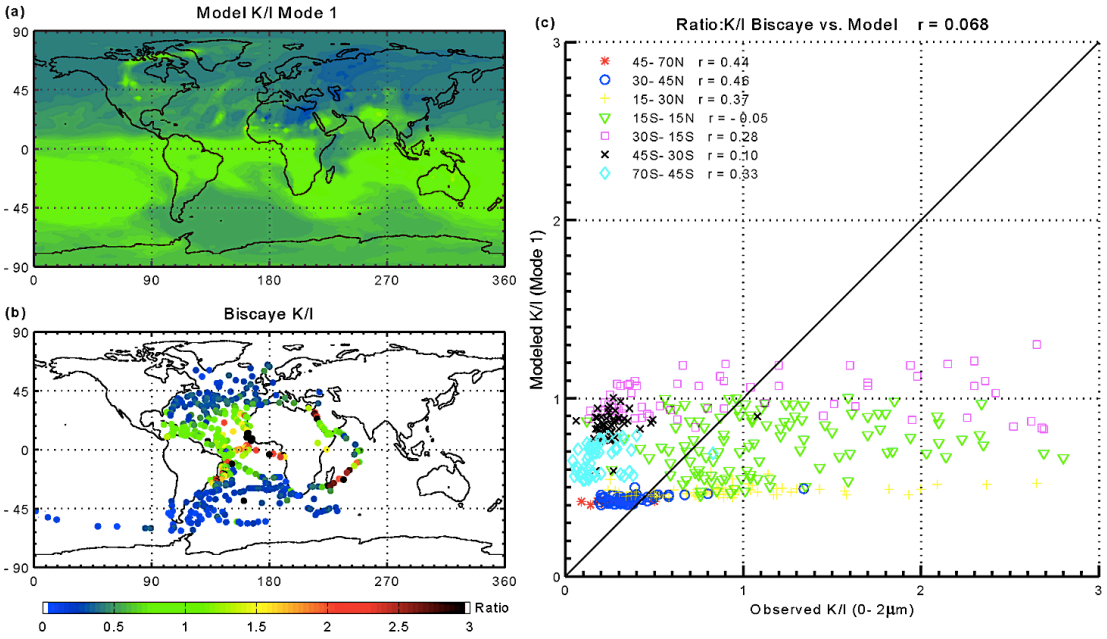

Figure 8: Kaolinite/Illite mineral ratio of wet and dry deposition for mode 1 from CAM5 (a) (kg K/kg I) and from characteristic basal X-ray diffraction maxima ratios of K/I of ocean core sediments (b) (Biscaye 1965). Data is segregated by latitude bands in scatterplot (c).

3.2 Aerosol Optical Depth and Single Scattering Albedo

Aerosol optical depth (AOD), absorbing aerosol optical depth (AAOD) and single scattering albedo (SSA) are simulated for each model and compared to AERONET retrievals. AERONET sites were chosen in regions where the modeled $AOD_{dust} > AOD_{total} \times 0.5$ to restrict the comparison to dust. The total AOD depends on the concentration of suspended aerosols and the degree to which they attenuate radiation. For both CAM4 and CAM5, the simulations with mineralogy have smaller values compared to the simulations with tuned dust at nearly every point (Figure 9a,b). This is due to the shortwave extinction coefficients for tuned dust having higher values than the extinction coefficients for each of the minerals. Both the simulations with tuned dust and with mineralogy are biased low and their range is about half that observed (Figure 9a,b). The simulations with mineralogy perform worse than those with tuned dust (Table 6) when comparing mean and range for AOD. The comparison for AAOD is poor in CAM4 however CAM5-m matches observations reasonably well with a predicted range larger than observed (Table 6b). CAM4-t and CAM5-t are more accurate at capturing the mean observed SSA across many sites while CAM4-m performs worse than CAM5-m (Figure 9e,f). CAM4-m is biased high and has decreased range of variability and less correlation than CAM4-t (Table 6). CAM5 overall is dustier with 5.7% of gridcells meeting $AOD_{dust} > 0.5*AOD_{total}$, and 32.4% of these have column hematite percents greater than 1.5%. In contrast, CAM4-m has 40% fewer "dusty" gridcells and only 12.4% of these containing total column hematite percents above 1.5%. While CAM5-t does well in matching AERONET SSA. CAM5-m predicts lower SSA and a greater range than observed (Figure 9f).

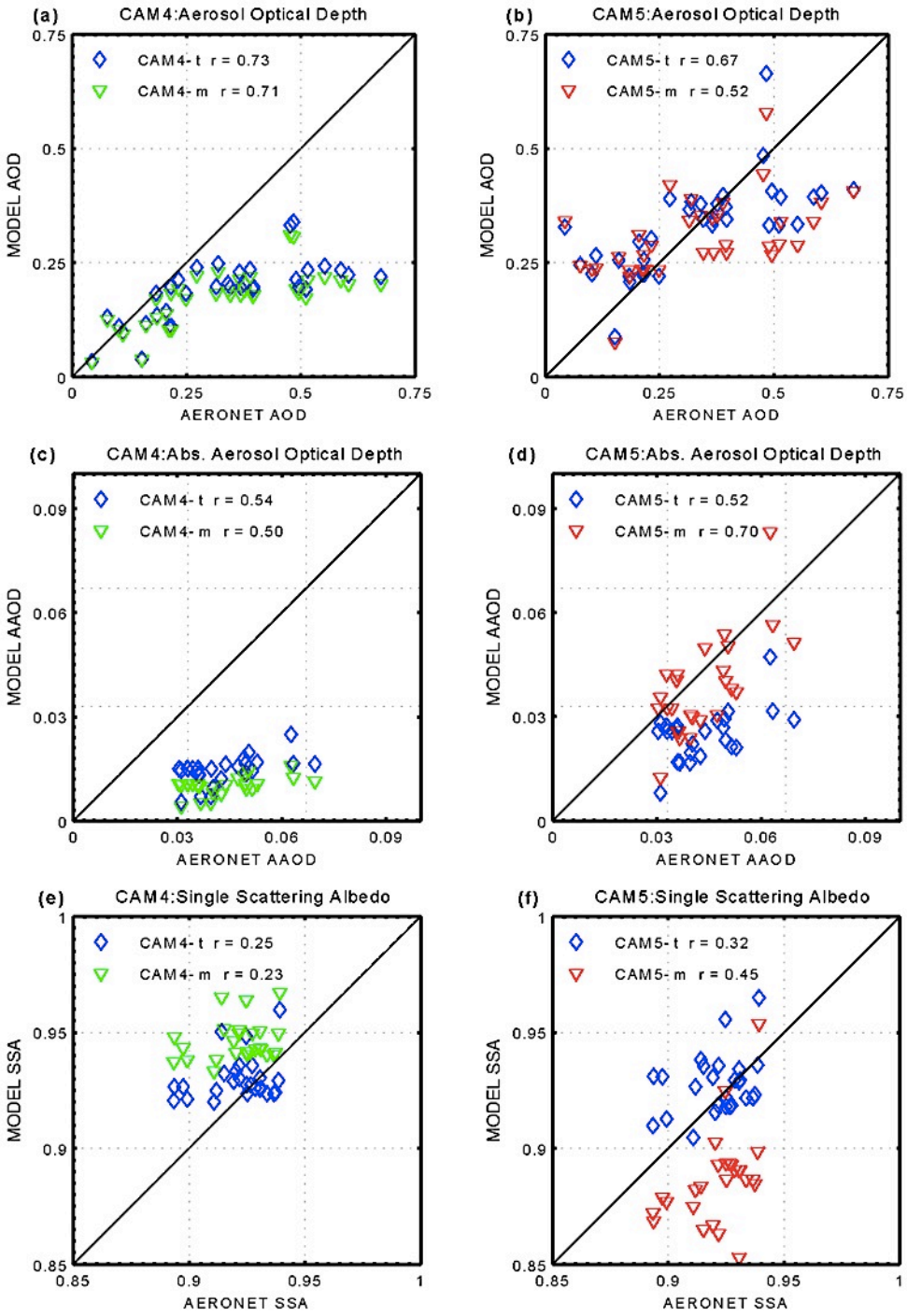

Figure 9: Modeled Aerosol Optical Depth (a,b), Absorbing Aerosol Optical Depth (c,d) and Single Scattering albedo (e,f) compared to AERONET retrievals at sites where modeled $AOD_{dust} > AOD_{total}*0.5$. CAM4 (a,c,e) and CAM5 (b,d,f) are shown.

Table 6a: The mean and standard deviation for AERONET (Holben et al., 1998, 2001) retrivals and the mean for CAM4 with tuned dust (CAM4-t) and mineralogy (CAM4-m) and CAM5 with tuned dust (CAM5-t) and mineralogy (CAM5-m) for Aerosol Optical Depth, Absorbing Aerosol Optical Depth and Single Scattering Albedo at AERONET sites where $AOD_{dust} > 0.5*AOD_{total}$

		AOD	AAOD	SSA
AERONET		0.332	0.043	0.921
	std	0.164	0.011	0.014
CAM4-t		0.187	0.015	0.930
CAM4-m		0.174	0.010	0.946
CAM5-t		0.330	0.025	0.927
CAM5-m		0.307	0.038	0.887
CAM4-trs		0.233	0.015	0.942
CAM5-trs		0.384	0.027	0.932

Table 6b: The standard deviation in the model over the standard deviation in AERONET. Values less than 1 indicate that the model is not capturing the dynamic range from the observations while values greater than 1 indicate the model is simulating a larger range than observed. This metric is used to test whether the simulations with mineralogy are better capturing the range in the observations, with blue denoting a decrease in ability and red signifying an increase.

	AOD	AAOD	SSA
CAM4-t	0.40	0.37	0.67
CAM4-m	**0.36**	**0.28**	**0.59**
CAM5-t	0.60	0.68	0.96
CAM5-m	**0.52**	**1.31**	**1.48**
CAM4-trs	0.54	0.38	0.53
CAM5-trs	0.93	0.93	0.87

Adding mineralogy to CAM4 does not seem to improve the simulation of AERONET AOD, AAOD, and SSA, whereas it does marginally in CAM5. The reason that adding mineralogy to CAM5 adds to the quality of the simulation at the

AERONET sites is because of the higher amounts of dust, as well as more hematite (Figure 10 and 11). Black carbon is a more efficient absorber than hematite (SSA = 0.17 vs 0.6). Black carbon is three times more abundant in CAM4-m than CAM5-m in dust dominated regions and it dominates the SSA signal (Figure 10 and 11).

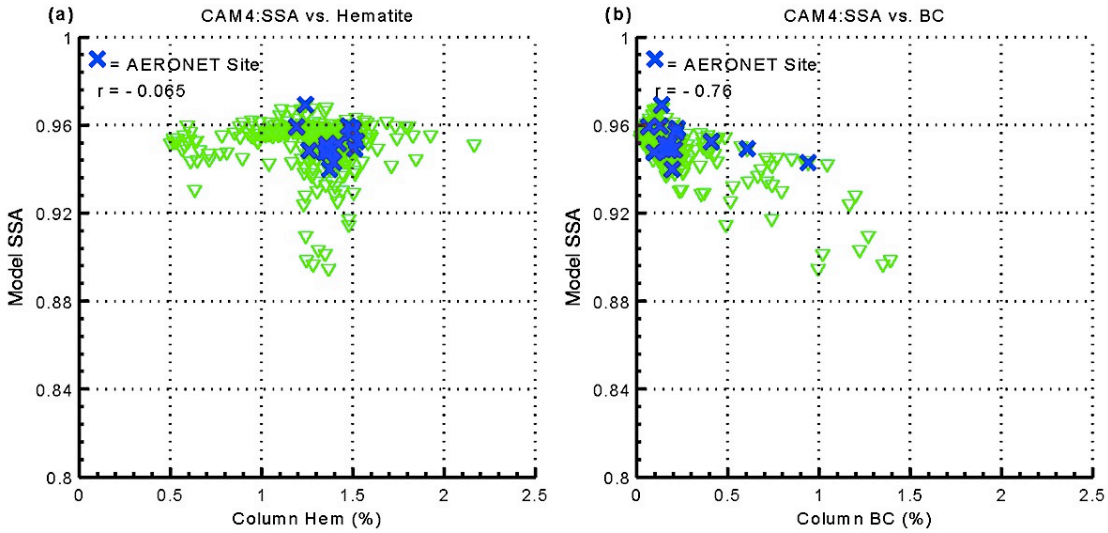

Figure 10: Model Single Scattering Albedo in CAM4 mineralogy is compared to total percent column hematite (a) and total percent column black carbon (b). The location of AERONET sites used in the comparison in Figure 9 are plotted in blue.

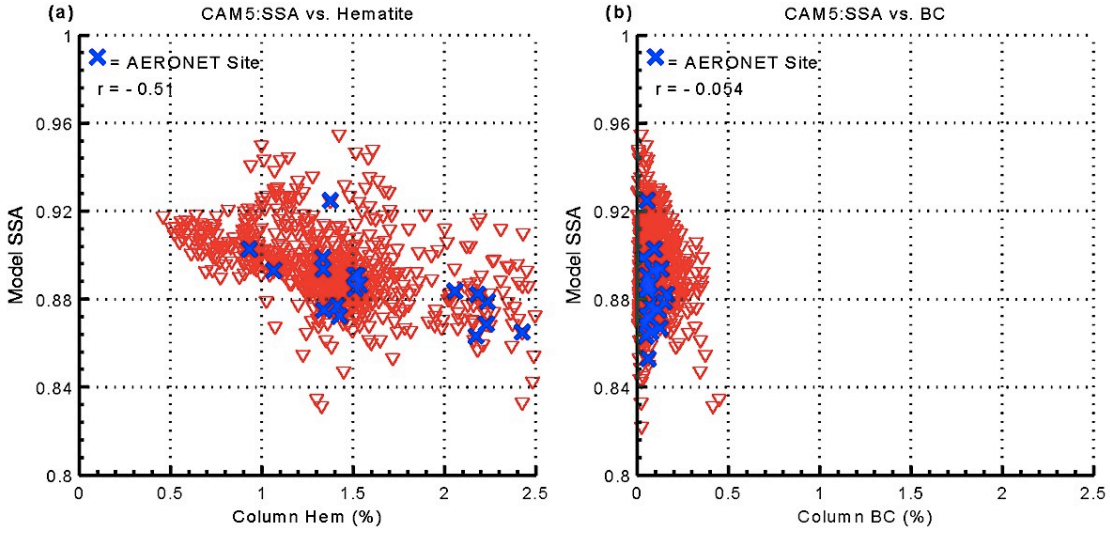

Figure 11: Model Single Scattering Albedo from CAM5 with mineralogy is compared to total percent column hematite (a) and total percent column black carbon (b). The location of AERONET sites used in the comparison in Figure 9 are plotted in blue.

The lower black carbon concentrations may be due to some problems with BC aging in CAM5 (Zhou et al., 2012). Recognize that while the aerosol forcing datasets were similar for both simulations, the simulations of CAM4 and CAM5 have many differences in meteorology, both because the physics included in the model is different as well as the way the models are forced (Section 2.1). Overall, inclusion of mineralogy did not improve comparisons at AERONET stations for AOD, AAOD and SSA.

3.3 Radiative Forcing

3.3.1 Clear-sky Radiative Forcing

The TOA radiative forcing efficiency ($Wm^{-2}\tau^{-1}$) of dust is compared to clear-sky satellite based observations over N. Atlantic (Li et al., 2004) and the Sahara (Zhang and Christopher, 2003;Patadia et al., 2009) for both simulations with tuned dust and mineralogy in CAM4 and CAM5 (Table 7). Out of the three shortwave observations considered, CAM4-t matches two of the observations better than CAM4-m. The clear-sky forcing efficiency observed by Li et al. 2004 during June, July and August (JJA) over the N. Atlantic is captured by CAM4-t, while CAM4-m simulated a smaller forcing. Extinction coeffiecient of tuned dust is larger than that of individual minerals; the refractive indices of tuned dust were calculated based on Maxwell-Garnet internal mixture of non-absorbing clays and quartz and absorbing hematite. The real portion (scattering) and the imaginary portion (absorbing) of the refractive index at 500nm is larger for tuned dust than for each of the minerals except for hematite. Hematite has much larger imaginary and real portions however the density of hematite is twice as large as the densities for tuned dust and for each of the minerals. Since the mass extinction efficiency is a factor of 1/density, hematite has a smaller mass extinction efficiency than all of the minerals.

Table 7: Comparison of observed top of atmosphere clear-sky radiative forcing efficiencies ($Wm^{-2}\tau^{-1}$) over N. Atlantic and N. Africa regions with simulated RFE. Simulations are for CAM4 and CAM5 with release dust, tuned dust, tuned dust and release size distribution, and mineralogy.

Reference; domain	Li et. al. 2004; 15-25 N, 45-15 W	Li et. al. 2004; 15-25 N, 45-15 W	Zhang and Christopher 2004; 15-35N,18W-40E	Patadia et. al. 2009; 15-30N,30E-10W
Observed	TOA:SW (JJA) **-35 ± 3**	TOA:SW (NDJ) **-26 ± 3**	TOA:LW (Sept.) **15**	TOA:SW (JJA) **0** (albedo = 0.4)
CAM4:Tuned	-32.0	-32.2	8.9	3.0
CAM4:Mineralogy	-26.4	-25.7	9.9	10.6
CAM5:Tuned	-28.2	-29.7	9.0	-0.3
CAM5:Mineralogy	-20.3	-22.2	7.8	10.5
CAM4:Tuned-rs	-30.4	-30.0	6.8	-2.0
CAM5:Tuned-rs	-29.8	-32.1	7.9	-2.3

The reason that CAM4-m has a smaller forcing efficiency is that for similar dust and mineral loads, the amount of radiation scattered back to space is dominated by the greater extinction efficiency of tuned dust, e.g tuned dust results in 13% more extinction per unit mass than mineralogy. For the "low" dust season, November, December and January (NDJ), the same phenomena is observed where with similar dust and mineral loads, tuned dust results in a more negative forcing efficiency at TOA for the CAM4-t case. However in this case, CAM4-m more closely matches the observation; however, the significance of this is not clear as clear-sky measurements during winter may be capturing black carbon from biomass burning as well as dust (Li et al., 2004).

CAM5-t and CAM5-m both underestimate the SW forcing efficiency observed by Li et al. (2004) although CAM4-t more closely matched this (Table 7). The reason for this is that mineralogy is significantly more absorbing with higher column concentrations of hematite, despite similar loading and optical depths (Figure 3d). Over the same domain but for the low dust season, CAM-t and CAM5-m loads are significantly different, 0.47 and 0.29 Tg respectively with optical depths, 0.07 and 0.04. While both fall within the range of the observation, CAM5-t simulates a more negative TOA forcing than CAM5-m since there is a higher concentration of dust available to scatter incoming radiation back out.

The clear-sky forcing efficiency over North Africa is approximately 0 in the observations for an albedo of 0.4 during "high" dust season (JJA) (Patadia et al., 2009). Both CAM4 and CAM5 simulations with tuned dust match the observations better than the simulations with mineralogy. Over N. Africa, there are competing mechanisms for the TOA forcing efficiency in both reality and modeling. Tuned dust in CAM4 is more absorbing than CAM4-m however it is also more efficient at scattering incoming SW radiation. In addition to scattering more incoming radiation (cooling at TOA), it will also absorb more SW radiation reflected from the surface (warming at TOA). CAM4-t is not as efficient at scattering incoming solar radiation and results in less cooling at the surface. Since TOA forcing is the sum of forcing at the surface and in the atmosphere, the smaller cooling from CAM4-m and similar atmospheric heating for both CAM4-t and CAM4-m results in an increased positive forcing at TOA for CAM4-m. In CAM5, the simulation with mineralogy has relatively high concentrations of hematite in this region (Figure 3d, Figure 11a) hence low SSA (Figure 12), and absorbs both incoming solar radiation and reflected SW radiation; for similar loads and optical depths, CAM5-m simulates increased surface

cooling and twice as much heating in the atmosphere, explaining the net positive SW forcing at TOA.

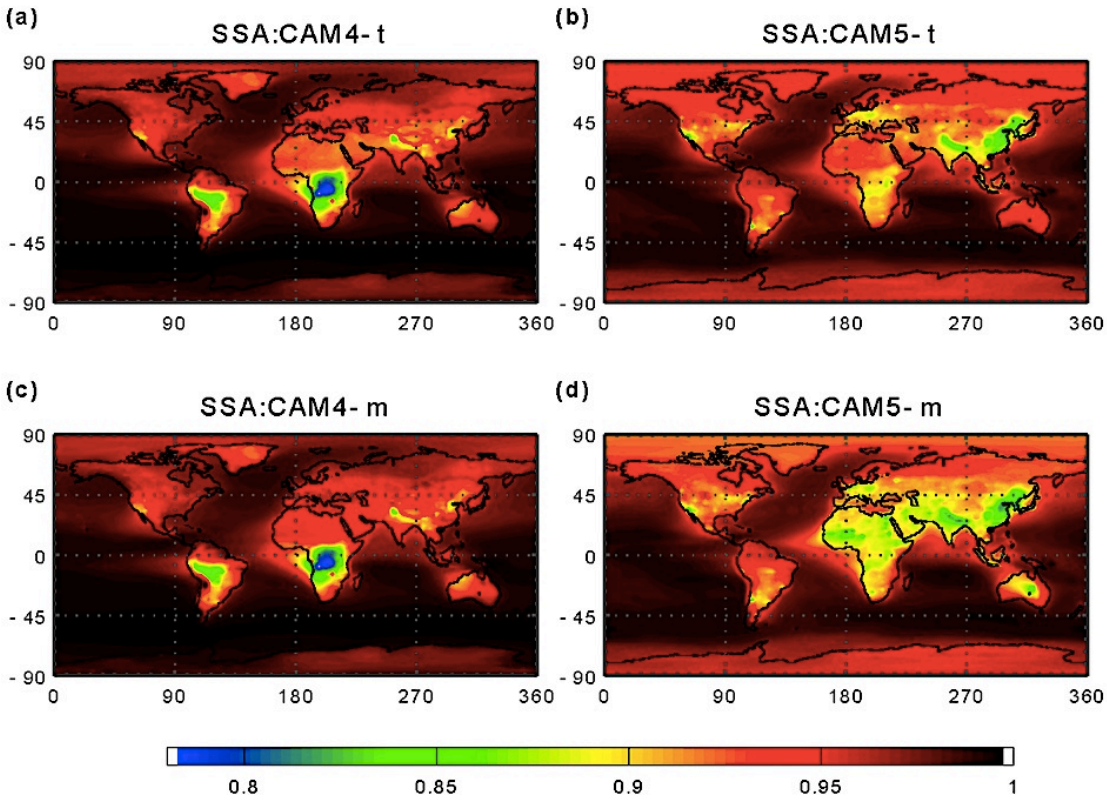

Figure 12: Model Single Scattering Albedo for CAM4 with tuned dust (a), CAM5 with tuned dust (b), CAM4 with mineralogy (c), and CAM5 with mineralogy (d).

Both CAM4 and CAM5 underestimate the clear-sky LW forcing efficiency observed by Zhang and Christopher (2004) over N. Africa in September. The difference between CAM4-m and CAM4-t is not meaningful since the same LW optical properties were prescribed for both tuned dust and mineralogy. CAM5-m does worse than CAM5-t for this observation. For CAM5-m, the clay minerals and hematite were the only minerals included, and the silt-sized minerals such as quartz and calcite were not explicitly modeled. Quartz dominates absorption in the IR spectrum with additional significant contributions from both the silt-sized and clay

minerals (Sokolik and Toon, 1999). CAM5-m is not capturing the quartz signal or the other silt-sized mineral signals, and thus it simulates less surface heating and a smaller LW TOA forcing. The simulations of dust and mineralogy in CAM4 and CAM5 only account for absorption in the LW and exclude scattering which has been shown to underestimate the LW forcing by up to 50% at TOA and 15% at the surface (Dufresne et al., 2002) and serves to explain why both models underestimate the observed forcing.

3.3.2 All-sky Radiative Forcing

All-sky radiative forcing is a delicate balance between heating and cooling of SW and LW radiation (Table 8, Figure 13 and 14). The difference between tuned dust and mineralogy for the all-sky TOA radiative forcing spatial distribution for CAM4 (Figure 13a,c) indicates intensified heating over desert and less cooling everywhere else. This is consistent with the more absorbing nature of tuned dust whose optical properties represent an internal mixture of minerals compared with mineralogy with combined optics of the external mixing of illite, kaolinite, montmorillonite, feldspar and hematite, along with an internal mixture of calcite, montmorillonite, quartz and illite; the result for CAM4-t being increased surface cooling with nearly identical atmospheric forcings and an overall, albeit small, net cooling compared to the small overall net warming from CAM4-m. On the other hand, the spatial pattern for CAM5-m indicates an intensification of heating over source regions, largely due to the SW atmospheric heating from hematite's absorption of both incoming and reflected SW radiation (Figure 13d, Figure 3d, Table 8b). Over bright reflective surfaces such as desert, higher column concentrations of hematite in CAM5-m absorb incoming solar radiation as well as SW radiation reflected by the high-albedo surface resulting in less solar radiation being reflected back out at TOA. While the larger absorption of

incoming solar radiation of CAM5-m does not change the SW forcing at TOA, the absorption of reflected SW does affect this, and over desert, it is clear that both these processes are resulting in a positive atmospheric forcing twice as large as the cooling at the surface (Table 8b).

Table 8a: Simulated annual average all-sky radiative forcing.

Model	Type	τ	TOA	TOA(SW)	TOA(LW)	ATM	ATM(SW)	ATM(LW)	SFC	SFC(SW)	SFC(LW)
CAM4	tuned	0.0148	-0.05	-0.13	0.08	0.20	0.51	-0.30	-0.25	-0.63	0.38
CAM4	mineral	0.0131	0.04	-0.04	0.08	0.20	0.50	-0.30	-0.16	-0.54	0.38
CAM5	tuned	0.0274	-0.11	-0.30	0.19	0.25	0.78	-0.53	-0.36	-1.09	0.72
CAM5	mineral	0.0267	0.10	-0.05	0.15	0.74	1.22	-0.48	-0.64	-1.28	0.64
CAM4	tuned-rs	0.0206	-0.13	-0.22	0.08	0.21	0.51	-0.31	-0.34	-0.73	0.39
CAM5	tuned-rs	0.0324	-0.26	-0.45	0.19	0.24	0.82	-0.58	-0.49	-1.27	0.77

Table 8b: Simulated regional annual average all-sky radiative forcing. For comparison, regions are from Yoshioka et al. 2007.

	Model	TOA	TOAsw	TOAlw	ATM	ATMsw	ATMlw	SFC	SFCsw	SFClw	AOD
N. Atlantic; 0°-30°N, 50°-20°W	CAM4	-0.12	-0.23	0.11	1.13	1.32	-0.20	-1.24	-1.55	0.31	0.04
	CAM4-m	0.05	-0.07	0.11	1.02	1.22	-0.20	-0.97	-1.28	0.31	0.03
	CAM5	-1.03	-1.42	0.39	1.24	1.91	-0.67	-2.26	-3.33	1.06	0.08
	CAM5-m	-0.25	-0.60	0.35	2.89	3.49	-0.60	-3.14	-4.09	0.95	0.08
N. Africa; 5°-35°N, 18°W-40°E	CAM4	-0.06	-1.19	1.13	2.08	7.61	-5.53	-2.14	-8.80	6.66	0.21
	CAM4-m	1.17	0.02	1.15	2.04	7.61	-5.57	-0.87	-7.60	6.73	0.18
	CAM5	0.33	-2.21	2.54	2.94	11.38	-8.45	-2.61	-13.59	10.98	0.37
	CAM5-m	3.17	1.16	2.01	9.38	17.31	-7.93	-6.21	-16.14	9.94	0.36
W. Indian Ocean; 10°S-15°N, 50°-70°E	CAM4	-0.71	-1.15	0.44	1.10	2.55	-1.45	-1.81	-3.70	1.89	0.08
	CAM4-m	-0.19	-0.64	0.45	1.03	2.49	-1.46	-1.22	-3.13	1.91	0.07
	CAM5	-0.88	-1.65	0.77	1.32	3.66	-2.35	-2.20	-5.31	3.11	0.14
	CAM5-m	0.21	-0.45	0.66	4.31	6.60	-2.29	-4.10	-7.05	2.95	0.15

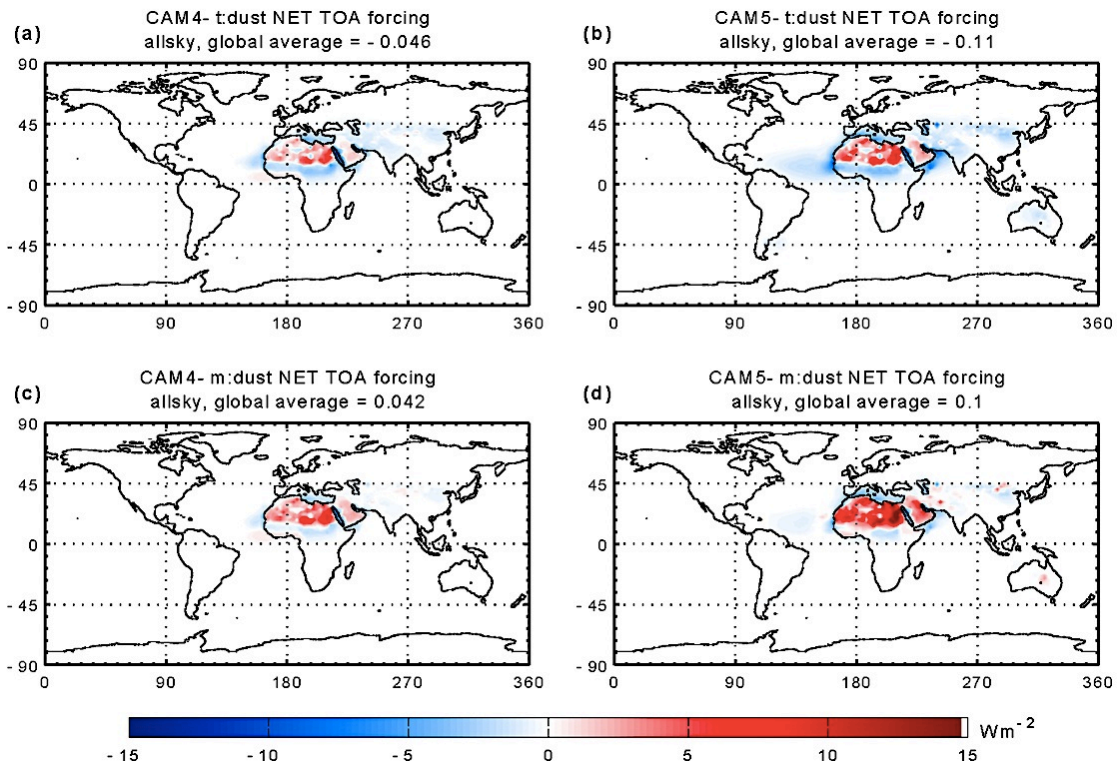

Figure 13: Spatial distribution of annual all-sky radiative forcing (SW+LW) at the top of atmosphere for CAM4 with tuned dust and with mineralogy (a,c) and for CAM5 with tuned dust and mineralogy (b,d).

Net surface forcing for CAM4-t, CAM4-m and CAM5-t have similar spatial patterns as TOA forcing, however, CAM5-m indicates much greater surface cooling everywhere (Figure 13). In the three major regions contributing to RF from dust, N. Atlantic, N. Africa, W. Indian Ocean (Yoshioka et al., 2007), the changes between mineralogy and tuned dust are dominated by SW forcing (Table 8b).

To summarize, there are two different mechanisms for increased positive TOA forcing for both models with mineralogy. For CAM4, while the SSA is higher for mineralogy, the overall extinction efficiency is higher for tuned dust, largely due to the fact that the optical properties for tuned dust are simulated as an internal mixture. For CAM5, both dust and mineralogy is internally mixed with other aerosol species, however the SSA for mineralogy is much lower due to the high concentrations of hematite over key regions contributing to the global RF from dust. While it is not

clear that mineralogy improves global dust RF, and in several observations appears to do worse, all four simulations fall within the range of previous RF modeling estimates (Yoshioka et al., 2007;Woodward, 2001;Miller et al., 2004;Miller et al., 2006).

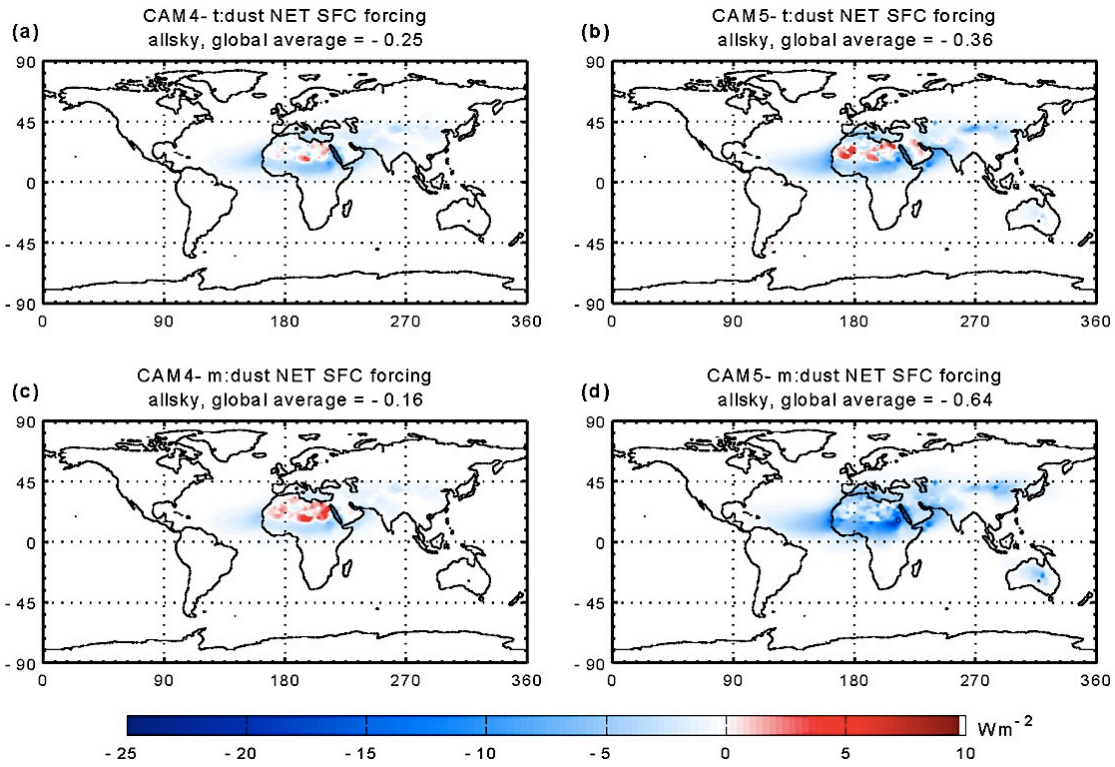

Figure 14: Spatial distribution of annual all-sky radiative forcing (SW+LW) at the surface for CAM4 with tuned dust and with mineralogy (a,c) and for CAM5 with tuned dust and mineralogy (b,d).

A comparison to radiative forcing efficiency from another study which included mineralogy (Balkanski et al., 2007) is not straightforward since that study inferred that the ideal hematite inclusion for an internal dust mixture twice the value in this study. For both CAM4 and CAM5 simulations with mineralogy, the hematite content in the soil distributions is 1.4% by mass, or, 0.7% by volume, while the tuned dust assumes 0.8% hematite by mass, or 0.4% by volume. For the case with 1.5% hematite by volume, they report TOA forcing efficiency which is too cooling compared to the clear-sky RFE reported by Li et al. 2004, while surface RFE matched

observations. From this, the atmospheric heating efficiency was underestimated. The results for clear-sky TOA forcing efficiency are less cooling in both CAM4-m and CAM5-m however the surface RFE in both cases is very similar to the observed -65±3 $Wm^{-2}\tau^{-1}$, -64 and -60 $Wm^{-2}\tau^{-1}$ respectively. Additionally, both cases with mineralogy come close to the estimated atmosphere heating efficiency of 30 ±4 $Wm^{-2}\tau^{-1}$, with values of 38 and 34 $Wm^{-2}\tau^{-1}$ for CAM4-m and CAM5- m respectively.

3.4 Sensitivity to Size

Changes in optics are most important in determining all-sky DRF, with size and mineralogy following with comparable importance in CAM4 and with mineralogy and then size in CAM5 (Table 9). Comparing to clear-sky DRE observations, the order of importance is less clear with CAM4 with tuned optics, scavenging and release size distribution (CAM4-trs) doing worse (-30.4 $Wm^{-2}\tau^{-1}$) than CAM4-t (-32.0 $Wm^{-2}\tau^{-1}$) over N. Atlantic JJA and better (-30.0 $Wm^{-2}\tau^{-1}$) during NDJ than CAM4-t (-32.2 $Wm^{-2}\tau^{-1}$) (Table 7). Comparing to observations from Patadia et al. 2009, both CAM4-trs and CAM5-trs overcompensates the cooling efficiency while both CAM4-m and CAM5-m undercompensate (Table 7). In general, the higher concentrations of small particles in the simulations using release sizes result in increased reflectivity and increased cooling at TOA. For clear-sky observations, it appears that size is more important than mineralogy, and in comparable importance to optics.

Comparing to AERONET retrievals, higher correlations are calculated for CAM4-trs and CAM5-trs compared to the tuned cases for AOD, AAOD. The correlation for SSA is the same between CAM4-t and CAM4-trs, while the correlation is higher for CAM5-trs than CAM5-t (Figure 15). Despite this, the size distribution of dust derived from AERONET more closely matches the size distribution derived from Kok et al. 2011.

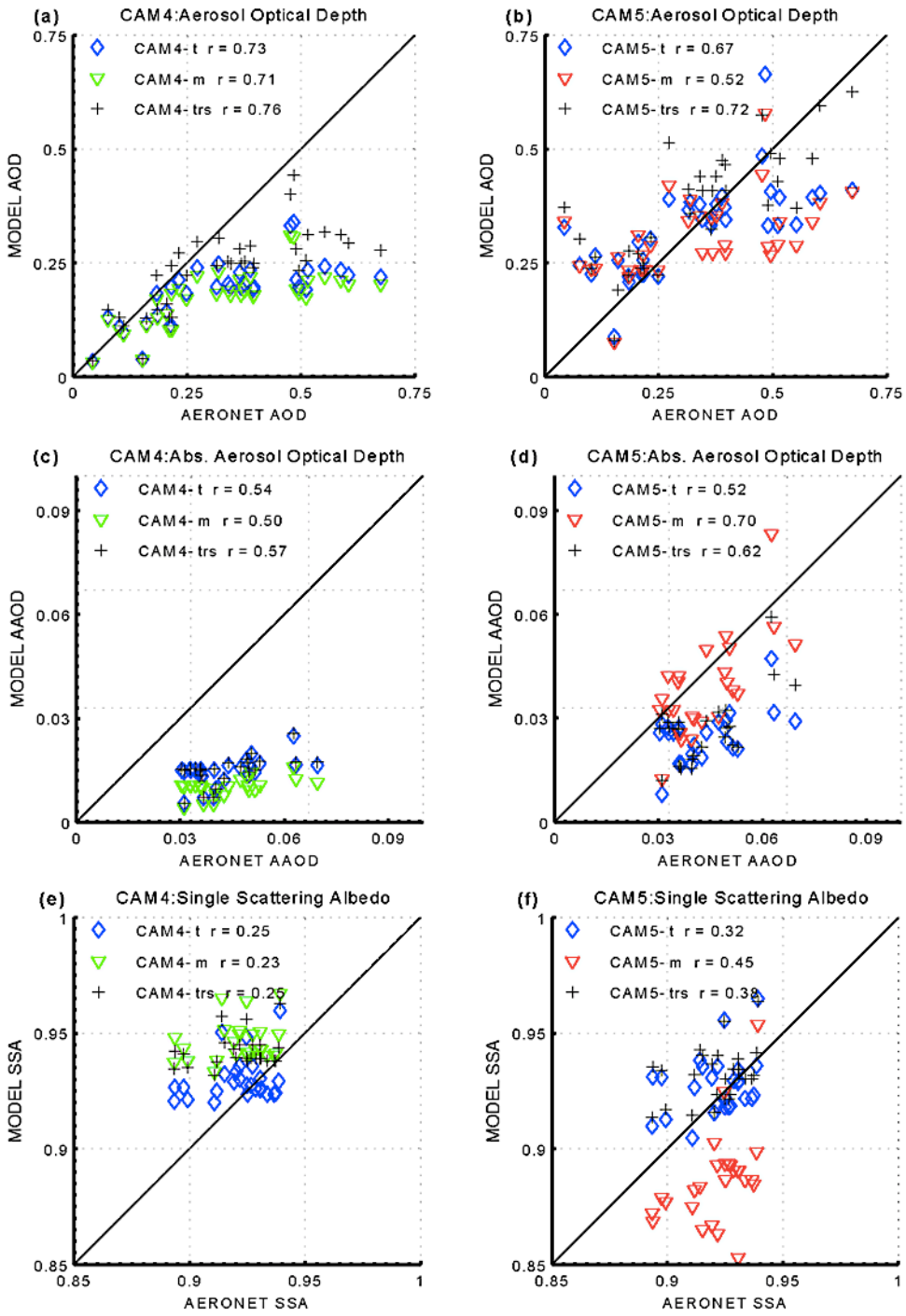

Figure 15: Modeled Aerosol Optical Depth (a,b), Absorbing Aerosol Optical Depth (c,d) and Single Scattering albedo (e,f) compared to AERONET retrievals at sites where modeled $AOD_{dust} > AOD_{total}*0.5$. CAM4 (a,c,e) and CAM5 (b,d,f) are shown for tuned dust, mineralogy, and tuned dust + release size.

Overall, including mineralogy is comparable to changes in size and optics when comparing to AERONET however, when comparing to radiative forcing, it is less clear whether including mineralogy is as important as optics or size changes.

Table 9: Percent change in annual all-sky radiative forcing for CAM4 and CAM5 from tuned to tuned + release size, tuned to mineralogy and tuned + release size to mineralogy.

percent change	TOA	TOA(SW)	TOA(LW)	ATM	ATM(SW)	ATM(LW)	SFC	SFC(SW)	SFC(LW)
4t→trs	160.0%	69.2%	0.0%	5.0%	0.0%	3.3%	36.0%	15.9%	2.6%
4t→m	-180.0%	-69.2%	0.0%	0.0%	-2.0%	0.0%	-36.0%	-14.3%	0.0%
5t→trs	136.4%	50.0%	0.0%	-4.0%	5.1%	9.4%	36.1%	16.5%	6.9%
5t→m	-190.9%	-83.3%	-21.1%	196.0%	56.4%	-9.4%	77.8%	17.4%	-11.1%
4trs→m	-130.8%	-81.8%	0.0%	-4.8%	-2.0%	-3.2%	-52.9%	-26.0%	-2.6%
5trs→m	-138.5%	-88.9%	-21.1%	208.3%	48.8%	-17.2%	30.6%	0.8%	-16.9%

3.5 Quantifying Uncertainty

As this study is the first to simulate the radiative forcing by modeling the distribution of individual minerals in place of dust that we are aware of, it is not possible to compare the uncertainties in our model with those from another study. In an attempt to quantify the uncertainties associated with the mineralogy simulations, we identify the sources of error to estimate an upper bound uncertainty. From the mineral source maps derived from Claquin et al. 1999, the standard deviation in soil mineral content comprises up to 33% of the given mineral contents. Uncertainties from direct radiative forcing of dust based on simulations included in the Intergovernmental Panel on Climate Change (IPCC) have been previously estimated to be around 20% (Mahowald et al., 2010), which results from a combination of the uncertainty

associated with dust distribution and the radiative forcing calculation itself. We don't have enough data to estimate the uncertainties in the mineral optical properties, although it is clear that the refractive indices for a given mineral can vary due to imperfections or inclusions which may reflect the geographic location of minerals. Therefore, we are only able to make a rough estimate of the uncertainty in the direct radiative forcing from mineralogy of about 40%. The ability to reduce the uncertainty is limited by available mineralogy maps, and having the mineralogy at every location is currently not feasible even with remote sensing. Daily averaged values for elements in Zhang et al. in prep, which use the CAM4 mineralogy (multiple tracer) framework from this study, indicates that the soil spatial variability dominates the temporal variability. Since daily averaging didn't improve the elemental dynamic range, we likely would not see a significant improvement in mineral distribution variability by simulating daily output.

CHAPTER 4

4.0 DISCUSSION AND CONCLUSION

For the first time, the ability to carry multiple types of minerals instead of only a bulk dust has been included in both CAM4 and CAM5, and mineralogy is coupled to radiation to simulate the impacts on radiative forcing. In general, the mineral distributions simulated in CAM4 and CAM5 lack the dynamic variability that the few available observations indicate. Myriad reasons are responsible, including the averaged mineral source maps used in the simulations, the very limited number of mineralogy observations, the much shorter averaging period for the observations compared to the model as well as the fact that atmospheric processing of minerals is not yet included in these models. Simulations with daily output could help with comparing mineralogy collected over the course of a dust event; however, new mineral source maps are needed along with chemical and physical atmospheric processing mechanisms to better match observations. Soil properties and mineralogy are likely to change on very short spatial scales in the real world, while the model assumes averages over large regions.

In order to best match aerosol optical depth, absorbing aerosol optical depth and single scattering albedo from AERONET, it is not clear that adding mineralogy improves the comparison (Figure 9). Sensitivity studies with size suggest that assumed size distributions are as important as the inclusion of mineralogy for correctly simulating the AERONET observations (Figure 15). Similarly inclusion of mineralogy also did not significantly improve the simulation of forcing efficiency compared to observations. Changes in the assumed size distribution were similarly important in forcing efficiency calculations.

For calculating globally averaged radiative forcing, the simulations with mineral speciation are as important as the assumed size distribution. The single scattering albedo of dust is likely to be close to the threshold, where the sign of radiative forcing and climate response changes with small changes in SSA (Perlwitz et al., 2001). In both the CAM4 and CAM5 simulations, including mineralogy caused the modeled radiative forcing to switch from a small negative value (-0.05 and -0.11 Wm^{-2} for CAM4 and CAM5 with tuned dust) to a small positive value (+0.04 and +0.10 Wm^{-2} for CAM4 and CAM5 with mineralogy). Notice that our results are sensitive to the poorly constrained simulation of mineralogy; improvements in the simulation of mineralogy could change the importance of mineralogy to aerosol properties and forcing.

In conclusion, more work is needed to improve input mineral source maps as well as mechanisms to simulate atmospheric processing. While mineralogy was not the most important factor for direct radiative forcing simulations in this model, mineralogy is likely to be important for soluble iron impacts on biogeochemistry (Journet et al., 2008), as well as for aerosol-cloud interations (Yin et al., 2002;Koehler et al., 2009;Hoose et al., 2008), and with this paper we have constructed the speciation framework to investigate mineralogy effects on these processes.

BIBLIOGRAPHY

Albani, S., Mahowald, N., Perry, A., Scanza, R., Zender, C., and Flanner, M. G.: Improved representation of dust size and optics in the CESM, Geoscientific Model Development, submitted.

Balkanski, Y., Schulz, M., Claquin, T., and Guibert, S.: Reevaluation of mineral aerosol radiative forcings suggests a better agreement with satellite and AERONET data, Atmos. Chem. Phys, 7, 81-95, 2007.

Batjes, N.: A world dataset of derived soil properties by FAO–UNESCO soil unit for global modelling, Soil use and management, 13, 9-16, 1997.

Biscaye, P. E.: Mineralogy and sedimentation of recent deep-sea clay in the Atlantic Ocean and adjacent seas and oceans, Geological Society of America Bulletin, 76, 803-832, 1965.

Caquineau, S., Gaudichet, A., Gomes, L., Magonthier, M. C., and Chatenet, B.: Saharan dust: Clay ratio as a relevant tracer to assess the origin of soil-derived aerosols, Geophysical research letters, 25, 983-986, 1998.

Claquin, T., Schulz, M., and Balkanski, Y.: Modeling the mineralogy of atmospheric dust sources, Journal of Geophysical Research, 104, 22,243-222,256, 1999.

Coakley Jr, J. A., Cess, R. D., and Yurevich, F. B.: The effect of tropospheric aerosols on the earth's radiation budget: A parameterization for climate models, Journal of Atmospheric Sciences, 40, 116-138, 1983.

Conley, A., Lamarque, J.-F., Vitt, F., Collins, W., and Kiehl, J.: PORT, a CESM tool for the diagnosis of radiative forcing, Geoscientific Model Development, 6, 469-476, 2013.

Cwiertny, D. M., Baltrusaitis, J., Hunter, G. J., Laskin, A., Scherer, M. M., and Grassian, V. H.: Characterization and acid-mobilization study of iron-containing mineral dust source materials, Journal of Geophysical Research: Atmospheres (1984–2012), 113, 2008.

DeMott, P. J., Sassen, K., Poellot, M. R., Baumgardner, D., Rogers, D. C., Brooks, S. D., Prenni, A. J., and Kreidenweis, S. M.: African dust aerosols as atmospheric ice nuclei, Geophysical Research Letters, 30, 1732, doi:1710/1029/2003GL017410, 012003, 2003.

Dufresne, J.-L., Gauier, C., Ricchiazzi, P., and Rouquart, Y.: Longwave Scattering Effects of Mineral Aerosols, American Meteorlogical Society, 59, 1959-1966, 2002.

Fecan, F., Marticorena, B., and Bergametti, G.: Parameterization of the increase of the aeolian erosion threshold wind friction velocity due to soil moisture for arid and semi-arid areas, Annales Geophysicae-Atmosphere Hydrospheres and Space Sciences, 17, 149-157, 1999.

Ghan, S. J., and Zaveri, R. A.: Parameterization of optical properties for hydrated internally mixed aerosol, Journal of Geophysical Research: Atmospheres (1984–2012), 112, 2007.

Ginoux, P., Chin, M., Tegen, I., Prospero, J. M., Holben, B. N., Dubovik, O., and Lin, S.-J.: Sources and distribution of dust aerosols with the GOCART model, Journal of Geophysical Research, 106, 20255-20273, 2001.

Glaccum, R. A., and Prospero, J. M.: Saharan aerosols over the tropical North Atlantic—Mineralogy, Marine Geology, 37, 295-321, 1980.
Gomes, L., Bergametti, G., Coudé-Gaussen, G., and Rognon, P.: Submicron desert dusts: A sandblasting process, Journal of Geophysical Research: Atmospheres (1984–2012), 95, 13927-13935, 1990.

Han, Q., Moore, J. K., Zender, C., Measures, C., and Hydes, D.: Constraining oceanic dust depostion using surface ocean dissolved Al, Global Biogeochemical Cycles, 22, doi:10.1029/2007GB002975, 2008.

Holben, B., Eck, T., Slutsker, I., Tanre, D., Buis, J., Setzer, A., Vermote, E., Reagan, J., Kaufman, Y., and Nakajima, T.: AERONET—A federated instrument network and data archive for aerosol characterization, Remote sensing of environment, 66, 1-16, 1998.

Holben, B. N., Tanre, D., Smirnov, A., ECK, T. F., Slutsker, I., Abuhassan, N., Newcomb, W. W., Schafer, J. S., Chatenet, B., Lavenu, F., Kaufman, Y. J., Vande Castle, J., O'Neill, N. T., Pietras, C., Pinker, R. T., Voss, K., and Zibordi, G.: An emerging ground-based aerosol climatology:Aerosol optical depth from AERONET, Journal of Geophysical Research, 106, 12067-12097, 2001.

Hoose, C., Lohmann, U., Erdin, R., and Tegen, I.: The global influence of dust mineralogical composition on heterogeneous ice nucleation in mixed-phase clouds, Environmental Research Letters, 3, 025003, 2008.

Hurrell, J. W., M. M. Holland, S. Ghan, J. -F. Lamarque, D. Lawrence, W. H. Lipscomb, N. Mahowald, D. Marsh, P. Rasch, D. Bader, W. D. Collins, P. R. Gent, J. J. Hack, J. Kiehl, P. Kushner, W. G. Large, S. Marshall, S. Vavrus, and Vertenstein, M.: The Community Earth System Model: A Framework for Collaborative Research, Bulletin of the American Meteorological Society, in press.

Iacono, M. J., Delamere, J. S., Mlawer, E. J., Shephard, M. W., Clough, S. A., and Collins, W. D.: Radiative forcing by long-lived greenhouse gases: Calculations with the AER radiative transfer models, Journal of Geophysical Research: Atmospheres (1984–2012), 113, 2008.

IPCC: Summary for Policymakers, in: Climate Change 2007: The Physical Science Basis. Contribution of Working Group I to the Fourth Assessment Report of the Intergovernmental Panel on Climate Change, edited by: Solomon, S., Qin, D., Manning, M., Chen, Z., Marquis, M., B., A. K., M., T., and L., M. H., Cambridge University Press, Cambridge, UK and New York, NY, USA, 2007.

Jickells, T., An, Z., Andersen, K., Baker, A., Bergametti, G., Brooks, N., Cao, J., Boyd, P., Duce, R., Hunter, K., Kawahata, H., Kubilay, N., laRoche, J., Liss, P., Mahowald, N., Prospero, J., Ridgwell, A., Tegen, I., and Torres, R.: Global iron connections between dust, ocean biogeochemistry and climate, Science, 308, 67-71, 2005.

Joseph, J., Wiscombe, W., and Weinman, J.: The delta-Eddington approximation for radiative flux transfer, Journal of the Atmospheric Sciences, 33, 2452-2459, 1976.
Journet, E., Desbouefs, K., Caqineau, S., and Colin, J.-L.: Mineralogy as a critical factor of dust iron solubility, Geophysical Research Letters, 35, doi:10.1029/2007GL031589, 2008.

Kalashnikova, O., and Kahn, R. A.: Mineral dust plume evolution over the Atlantic from MISR and MODIS aerosol retrievals, Journal of Geophysical Research, 113, doi:10.1029/2008JD010083, 2008.

Kandler, K., Schütz, L., Deutscher, C., Ebert, M., Hofmann, H., Jäckel, S., Jaenicke, R., Knippertz, P., Lieke, K., and Massling, A.: Size distribution, mass concentration, chemical and mineralogical composition and derived optical parameters of the boundary layer aerosol at Tinfou, Morocco, during SAMUM 2006, Tellus B, 61, 32-50, 2009.

Karydis, V., Kumar, P., Barahona, D., Sokolik, I., and Nenes, A.: On the effect of dust particles on global cloud condensation nuclei and cloud droplet number, Journal of Geophysical Research: Atmospheres (1984–2012), 116, 2011.

Koehler, K. A., Keidenweis, S., Demott, P., Petters, M., and al., A. P. e.: Hygroscopicity and cloud droplet activation of mineral dust aerosol, Geophysical Research Letters, 36:L08805, 2009.

Kok, J.: A scaling theory for the size distribution of emitted dust aerosols suggests climate models underestimate the size of the global dust cycle, Proceedings of the National Academy of Science USA, 108, 1016-1021, 2011.

Kolmogorov, A. N.: On the logarithmically normal law of distribution of the size of particles under pulverisation, Doklady Akademii Nauk SSSR, 31, 99-101, 1941.

Lamarque, J.-F., Emmons, L., Hess, P., Kinnison, D. E., Tilmes, S., Vitt, F., Heald, C., Holland, E. A., Lauritzen, P., and Neu, J.: CAM-chem: description and evaluation of interactive atmospheric chemistry in the Community Earth System Model, Geoscientific Model Development, 5, 369-411, 2012.

Levin, Z., Teller, A., Ganor, E., and Yin, Y.: On the interactions of mineral dust, sea-salt particles, and clouds: A measurement and modeling study from the Mediterranean Israeli Dust Experiment campaign, Journal of geophysical research, 110, D20202, 2005.

Li, F., Vogelman, A., and Ramanathan, V.: Saharan dust aerosol radiative forcing measured from space, Journal of Climate, 17, 2558-2571, 2004.

Liu, X., Easter, R., Ghan, S., Zaveri, R., Rasch, P., Shi, X., Lamarque, J.-F., Gettelman, A., Morrison, H., Vitt, F., Conley, A., Park, S., Neale, R., Hannay, C., Eckman, A., Hess, P., Mahowald, N., Collins, W., Iacono, M., Bretherton, C., Flanner, M., and Mitchell, D.: Toward a minimal representation of aerosol direct and indirect ef fects: model description and evaluation, Geoscientific Model Development Discussions, 4, 3485-3598, 2011.

Mahowald, N., and Kiehl, L.: Mineral aerosol and cloud interactiocns, Geophysical Research Letters, 30, 10.109/2002GL016762, 2003.

Mahowald, N., D. Muhs, Levis, S., Rasch, P., Yoshioka, M., and Zender, C.: Change in atmospheric mineral aerosols in response to climate: last glacial period, pre-industrial, modern and doubled-carbon dioxide climates Journal of Geophysical Research, 111, D10202, doi:10210.11029/12005JD006653, 2006.

Mahowald, N., Kloster, S., Engelstaedter, S., Moore, J. K., Mukhopadhyay, S., McConnell, Albani, S., Doney, S., Bhattacharya, A., Curran, M., Flanner, M., Hoffman, F., Lawrence, D., Lindsay, K., Mayewski, P., Neff, J., Rothenberg, D., Thomas, E., Thornton, P., and Zender, C.: Observed 20th century desert dust variability: impact on climate and biogeochemistry, Atmospheric Chemistry and Physics, 10, 10875-10893, 2010.

Martin, J., Gordon, R. M., and Fitzwater, S. E.: The case for iron, Limnology and Oceanography, 36, 1793-1802, 1991.

Miller, R., Tegen, I., and Perlwitz, J.: Surface radiative forcing by soil dust aerosols and the hydrologic cycle, Journal of Geophysical Research, 109, doi:10.1029/2003JD004085, 2004.

Miller, R., Cakmur, R., Perlwitz, J., Geogdzhayev, I., Ginoux, P., Kohfeld, K., Koch, D., Prigent, C., Ruedy, R., Schmidt, G., and Tegen, I.: Mineral dust aerosols in the NASA Goddard Institute of Space Sciences ModelE Atmospheric General Circulation Model, Journal of Geophysical Research, 111, doi:10.1029/2005JD005796, 2006.
Miller, R. L., and Tegen, I.: Climate Response to Soil Dust Aerosols, Journal of Climate, 11, 3247-3267, 1998.

Moosmüller, H., Engelbrecht, J. P., Skiba, M., Frey, G., Chakrabarty, R. K., and Arnott, W. P.: Single scattering albedo of fine mineral dust aerosols controlled by iron concentration, Journal of Geophysical Research: Atmospheres (1984–2012), 117, 2012.

Nickovic, S., Vukovic, A., Vujadinovic, M., Djurdjevic, V., and Pejanovic, G.: Technical Note: High-resolution mineralogical database of dust-productive soils for atmospheric dust modeling, Atmos. Chem. Phys, 12, 845-855, 2012.

Okin, G.: A new model of wind erosion in the presence of vegetation, Journal of Geophysical Research-Earth Surface, 113, doi:10.1029/2007JF000758, 2008.

Patadia, F., Yang, E.-S., and Christopher, S.: Does dust change the clear sky top of atmosphere shortwave flux over high surface reflectance regions?, Geophysical Research Letters, 36, doi:10.1029/2009GL039092, 2009.

Perlwitz, J., Tegen, I., and Miller, R.: Interactive soil dust aerosol model in the GISS GCM 1. Sensitivity of the soil dust cycle to radiative properties of soil dust aerosols, Journal of Geophysical Research, 106, 18,167-118,192, 2001.

Rasch, P. J., Feichter, H., Law, K., Mahowald, N., Penner, J., Benkovitz, C., Genthon, C., Giannakopoulos, C., Kasibhatla, P., Koch, D., Levy, H., Maki, T., Prather, M., Roberts, D. L., Roelofs, G.-J., Stevenson, D., Stockwell, Z., Taguchi, S., Chipperfield, M., Baldocchi, D., McMurry, P., Barrie, L., Balkanski, Y., Chatfield, B., Jacob, D., Kritz, M., Lawrence, M., Lee, H. N., Leaitch, R., Lelieveld, J., Noone, K. J., Seinfeld, J., Stenchikov, G., Schwarz, S., Walcek, C., and Williamson, D.: An Assessment of Scavenging and Deposition Processes in Global Models: Results from the WCRP Cambridge Workshop of 1995, Tellus, 52B, 1025-1056, 2000.

Reid, E., Reid, J., Meier, M., Dunlap, M., Cliff, S., Broumas, A., Perry, K., and Maring, H.: Characterization of African dust transported to Puerto Rico by individual particle and size segregated bulk analysis, JGR-Atmospheres, 108, doi:10.1029/1200dJD002935, 2003.

Sabre, M., Lopez, M., Alfaro, S., Rajot, J., and Gomes, L.: Characterization of the fine dust particle production process by wind erosion for two types of bare soil surfaces, Proceedings of Wind Erosion: An International Symposium/Workshop, 1997,

Seinfeld, J., and Pandis, S.: Atmospheric Chemistry and Physics, John Wiley and Sons, Inc, New York, 1326 pp., 1998.

Shen, Z., Li, X., Cao, J., Caquineau, S., Wang, Y., and Zhang, X.: Characteristics of clay minerals in Asian dust and their environmental significance, China Particuology, 3, 260-264, 2005.

Shi, Z., Shao, L., Jones, T., and Lu, S.: Microscopy and mineralogy of airborne particles collected during severe dust storm episodes in Beijing, China, Journal of Geophysical Research: Atmospheres (1984–2012), 110, 2005.

Siegel, D. A., and Deuser, W. G.: Trajectories of sinking particles in the Sargasso Sea: modeling of statistical funnels above deep-ocean sediment traps, Deep-Sea Research, 44, 1519-1541, 1997.

Sokolik, I. N., and Toon, O. B.: Incorporation of mineralogical composition into models of the radiative properties of mineral aerosol form UV to IR wavelengths, Journal of Geophysical Research, 104, 9423-9444, 1999.

Suarez, M. J., Rienecker, M., Todling, R., Bacmeister, J., Takacs, L., Liu, H., Gu, W., Sienkiewicz, M., Koster, R., and Gelaro, R.: The GEOS-5 Data Assimilation System-Documentation of Versions 5.0. 1, 5.1. 0, and 5.2. 0, 2008.

Swap, R., Garstang, M., Greco, S., Talbot, R., and Kallberg, P.: Saharan dust in the Amazon Basin, Tellus, 44B, 133-149, 1992.

Wiscombe, W. J.: Improved Mie scattering algorithms, Applied optics, 19, 1505-1509, 1980.

Woodward, S.: Modeling the atmopsheric life cycle and radiative impact of mineral dust in the Hadley Centre climate model, JGR, 106, 18,155-118,166, 2001.
Yin, Y., Wurzler, S., Levin, Z., and Reisin, T. G.: Interactions of mineral dust particles and clouds: Effects on precipitation and cloud optical properties, Journal of Geophysical Research: Atmospheres (1984–2012), 107, AAC 19-11-AAC 19-14, 2002.

Yoshioka, M., Mahowald, N., Conley, A., Collins, W., Fillmore, D., and Coleman, D.: Impact of desert dust radiative forcing on Sahel precipitation: relative importance of dust compared to sea surface temperature variations, vegetation changes and greenhouse gas warming, Journal of Climate, 20, 1445-1467, 2007.

Zender, C., Bian, H., and Newman, D.: Mineral Dust Entrainment and Deposition (DEAD) model: Description and 1990s dust climatology, Journal of Geophysical Research, 108, 4416, doi:4410.1029/2002JD002775, 2003.

Zhang, J., and Christopher, S.: Long wave radiative forcing of Saharan dust aerosols estimated from MODIS, MISR and CERES observations on TERRA, Geophysical Research Letters, 30, 2188, doi:2110.1029/2003GL018479, 2003.

Zhang, Y., Scanza, R., Mahowald, N., and Journet, E.: Elemental distribution from mineral aerosols, in prep.

Zhou, C., Penner, J. E., Flanner, M. G., Bisiaux, M. M., Edwards, R., and McConnell, J. R.: Transport of black carbon to polar regions: Sensitivity and forcing by black carbon, Geophysical Research Letters, 39, 2012.